Research Square

Preprints are preliminary reports that have not undergone peer review.
They should not be considered conclusive, used to inform clinical practice,
or referenced by the media as validated information.

Telocytes bridge acupuncture needling to biological responses by ITGB1- dependent mechanotransduction

Lu Mei
Nanjing Agricultural University
Meng Dai
Nanjing Agricultural University
Jianming Yue
Nanjing Agricultural University
Haixiang Huang
Nanjing Agricultural University
Zhenwei Zhang
Nanjing Agricultural University
Qiusheng Chen
chenqsh305@njau.edu.cn

Nanjing Agricultural University

Research Article

Keywords: CD34+/PDGFRα + telocytes, acupuncture, mechanical stretch, mechanotransduction, scRNA-seq, ITGB1, YAP, dorsal midline fascia

Posted Date: November 25th, 2026

DOI: https://doi.org/10.21203/rs.3.rs-11754055/v1

License: This work is licensed under a Creative Commons Attribution 4.0 International License.
Read Full License

Additional Declarations: No competing interests reported.

Telocytes bridge acupuncture needling to biological responses by ITGB1-dependent mechanotransduction

Lu Mei[1], Meng Dai[1], Jianming Yue[1], Haixiang Huang[1], Zhenwei Zhang[1], Qiusheng Chen[1*]

[1] College of Veterinary Medicine, Nanjing Agricultural University, Nanjing, China

*Correspondence to: Prof. Qiusheng Chen, E-mail: chenqsh305@njau.edu.cn

Abstract

Background: Acupuncture is a major therapeutic modality of traditional Chinese medicine for thousands of years, yet how the physical forces imposed by needling are transduced into biological responses remains largely elusive. This study aimed to investigate the structural basis and underlying molecular mechanisms of mechanotransduction in $CD34^{+}PDGFR\alpha^{+}$ telocytes (CPTCs) within mouse dorsal midline subcutaneous fascia (Sf).

Methods: Single-cell RNA sequencing, immunofluorescence, and electron microscopy were integrated to identify CPTCs in mouse dorsal midline Sf and characterize their mechanical-response signatures. Following acupuncture, single-cell profiling and morphological analyses were used to assess CPTC activation and subpopulation remodeling and infer changes in intercellular communication. Primary CPTCs were subjected to uniaxial stretch to model mechanical stimulation *in vitro*, with phenotypic alterations assessed by immunofluorescence, electron microscopy, flow cytometry, and migration assays. Quantitative proteomics and western blotting were applied to examine candidate ITGB1–FAK–ROCK2–YAP signaling. siRNA-mediated ITGB1 silencing was used to interrogate ITGB1-dependent mechanotransduction.

Results: CPTCs constituted the predominant cell population and exhibited pronounced responsiveness to mechanical stimuli in dorsal midline Sf. Histological imaging revealed coordinated mechanical linkage of CPTCs during needle manipulation. Both *in vivo* acupuncture and *in vitro* mechanical stretching activated CPTCs, as evidenced by increased microfilament cytoskeletal remodeling, proliferative activity, and intercellular communication. Single-cell profiling revealed an immediate-early gene program involving *Fos, Jun, and Atf3* in CPTC-C1. CPTC-C4 exhibited the strongest mechanical-response signature, accompanied by increased adhesion–cytoskeletal programs and higher *Itgb1* expression. Cyclic stretching *in vitro* further validated that CPTCs transduced mechanical cues via an ITGB1-dependent focal adhesion pathway

that activated FAK–ROCK2 signaling and promoted YAP nuclear translocation. ITGB1 silencing attenuated downstream FAK–ROCK2 signaling and CPTC activation, underscoring the indispensable function of ITGB1 in CPTC mechanosensing.

Conclusions: These findings support CPTCs as candidate initial mechanosensors that couple needle-induced mechanical forces to local biological responses through an ITGB1-dependent FAK–ROCK2–YAP axis, providing a new cellular perspective on the biological interpretation of acupuncture stimulation.

Keywords: CD34+/PDGFRα+ telocytes, acupuncture, mechanical stretch, mechanotransduction, scRNA-seq, ITGB1, YAP, dorsal midline fascia

1 Introduction

Acupuncture, a pivotal therapeutic intervention in traditional Chinese medicine, has been shown to exert anti-inflammatory [1] and immunomodulatory effects [2], thereby contributing to systemic homeostasis [3]. Research on acupuncture has largely focused on its downstream effects. A recent intravital imaging study using the RUSH3D-HR system provided direct visual evidence that electroacupuncture at Zusanli reduced the number of LPS-induced neutrophil swarming events in the mouse spleen [4]. Liu et al. identified PROKR2^Cre-marked sensory neurons as critical for transmitting low-intensity Zusanli stimulation to the vagal–adrenal axis [5]. These studies have advanced our understanding of the "effect" and "transmission" of acupuncture. Nevertheless, how the physical manipulation of needle twisting is converted into intracellular biological signals remains unresolved.

Increasing evidence indicates that the essence of acupuncture is a form of mechanical stimulation [6, 7]. In manual acupuncture, needle insertion and manipulation couple the needle to connective tissue, while rotation can wind collagen fibers around the needle and deform the surrounding matrix [8-11]. This coupling establishes a route for transmitting force, but understanding its biological consequences requires identifying the cells that sense extracellular matrix deformation and the mechanotransduction mechanisms through which they respond.

Telocytes (TCs) are specialized interstitial cells characterized by a small cell body and exceptionally long and thin telopodes under transmission electron microscopy [12]. Their extensive cellular networks and widespread entanglement with collagen fiber bundles underscore their intimate association with the fascial collagenous matrix [10, 11]. Beyond these structural associations, functional studies have implicated TCs in intercellular

communication and anti-inflammatory immunomodulation during acupuncture treatment [10]. Huang et al. implicated $CD34^{+}PDGFR\alpha^{+}$ TCs (CPTCs) in fascial macrophage remodeling during visceral inflammation and proposed a "fascia–visceral inflammatory crosstalk pattern" [13]. A recent study linked mechanosensitive $Ptgs2^{+}$ CPTCs to M2 macrophage activation via Il6–Il6st–Stat3 signaling, supporting a "force–immune axis" connecting acupuncture stimulation to anti-inflammatory responses [14]. Furthermore, one study in 2026 combining single-cell transcriptomics and interpretable deep learning has identified fascial CPTCs as prominent mechanosensors in the acupuncture treatment of a rat model of bacterial colitis. They defined a CPTC-Driven Mechano-Resonance Axis, where CPTCs serve as synchronized relay stations that convert somatic mechanical stimulation into systemic regenerative microenvironments [15]. Collectively, these findings position TCs as potential cellular mediators of somatic–visceral communication and acupuncture responses. However, the molecular mechanisms by which TCs sense mechanical forces at the cell–matrix interface and initiate intracellular mechanotransduction remain elusive.

Here, we investigated the structural and functional basis of TCs mechanotransduction in the subcutaneous fascia (Sf) of the mouse dorsal midline. We integrated multiscale imaging and single-cell transcriptomics to examine TC–collagen relationships and cellular responses to manual acupuncture. Complementary cyclic-stretch experiments in isolated TCs, together with proteomic analysis and gene silencing, were used to elucidate how TCs sense and transduce mechanical cues. By relating tissue-level mechanical coupling to cell-level sensing and functional responses, this study aims to clarify a local cellular mechanism through which the physical input of acupuncture can be translated into biological activity.

2 Materials and Methods

2.1 Mice

Twenty 8-week-old male C57BL/6J mice were purchased from Qinglongshan Experimental Animal Center (Nanjing, China). The mice were randomly assigned to the control group (CG) or acupuncture group (AG) (n = 10 per group). All animals were housed under specific pathogen-free conditions at the Laboratory Animal Center of Nanjing Agricultural University, with ad libitum access to food and water.

2.2 Acupuncture stimulation

Mice in the AG received acupuncture at two essential acupoints on the Governor

Vessel—Dazhui (GV14) and Mingmen (GV4) [16, 17]. GV14 and GV4 are located on the posterior midline as follows: GV14 in the depression below the spinous process of the seventh cervical vertebra, and GV4 in the depression below the spinous process of the second lumbar vertebra. Two sterilized stainless acupuncture needles (0.16 mm × 7 mm, Huabao Brand, Shenling Medical Equipment Co., Ltd., Wujiang, China) were inserted 2-3 mm into the acupoints at an angle of 15° to 30°. The needles were evenly twisted approximately 180° at a frequency of 60 times per minute for 1 min, manipulated every 5 min, and then withdrawn after 15 min. Acupuncture was administered once daily for 7 consecutive days.

2.3 Sample collection

Mice were euthanized by cervical dislocation after the 7-day acupuncture intervention. The dorsal midline region skin was fixed in 4% Paraformaldehyde (PFA) for histomorphometric evaluation, while 2.5% glutaraldehyde (pH adjusted to 7.4) was used for electron microscopy. Sf samples along the dorsal midline were collected as two biological replicates per group for single-cell RNA sequencing (scRNA-seq). All samples were obtained from a specific anatomical region along the dorsal midline. This rectangular area extended from point GV14 to 1 cm after point GV4 and had a width of 1 cm.

Needle-adherent tissue was collected following established protocols [18]. Briefly, needles were inserted at GV14 or GV4 and manipulated by lifting, thrusting, and twisting. Following manipulation, the needles were slowly and gently withdrawn, and the transparent tissue adhering to the needle surface was collected. Some tissue specimens were fixed together with their associated needles in 2.5% glutaraldehyde (pH 7.4) for scanning electron microscopy, whereas others were carefully detached from the needles and fixed in 4% PFA for subsequent morphological analysis.

2.4 H&E and Masson's trichrome staining

Skin samples were fixed in 4% PFA, embedded in paraffin, and sectioned at a thickness of 5 μm. H&E and Masson's trichrome staining were performed using standard protocols.

2.5 scRNA-seq

2.5.1 Tissue dissociation

Sf tissues were placed in sterile culture dishes containing ice-cold 1× Dulbecco's phosphate-buffered saline (DPBS; Thermo Fisher, Cat. no. 14190144) to remove residual storage solution and then minced on ice. Tissue fragments were enzymatically

digested with collagenase type IV (Sigma-Aldrich, Cat. no. C5138) and 10 μg/mL DNase I (Sigma, Cat. no. 11284932001) in PBS supplemented with 5% fetal bovine serum (FBS; Thermo Fisher, Cat. no. SV30087.02). Tissues were dissociated for approximately 40 min at 37°C with agitation at 50 rpm. Cell suspensions were passed through a 40-μm cell strainer, and red blood cells were removed using 1× Red Blood Cell Lysis Solution (Thermo Fisher, Cat. no. 00-4333-57). Dissociated cells were washed with 1× DPBS containing 0.4% FBS. Cell viability was assessed by 0.4% AO/PI staining using a Countstar Rigel S2 analyzer (Countstar, Shanghai). Samples with cell viability greater than 95% were subjected to subsequent scRNA-seq processing.

2.5.2 10× library preparation and sequencing

Single-cell suspensions were processed using a Chromium Controller, through which cells were encapsulated in gel bead-in-emulsion (GEM) droplets using a microfluidic system. Reverse transcription was performed to generate cDNA, followed by library preparation comprising fragmentation, adapter ligation, PCR amplification, and purification. All procedures were conducted in accordance with the manufacturer's instructions for the Chromium Single Cell 3′ v3.1 platform. The resulting libraries were quantified using a High Sensitivity DNA chip on a Bioanalyzer 2100 (Agilent) and a Qubit High Sensitivity DNA assay (Thermo Fisher Scientific). Libraries were sequenced on an Illumina NovaSeq 6000 platform using 2 × 150-bp paired-end chemistry. Sequencing and bioinformatic analyses were performed by Majorbio Co., Ltd. (Shanghai, China).

2.5.3 scRNA Data Analysis

The scRNA-seq data were analyzed on the online tool of Majorbio Cloud Platform (https://www.majorbio.com/tools). Raw sequencing data were processed using Cell Ranger (v10.0.0) to generate a gene-expression matrix. Subsequent analyses were conducted using Seurat (v5.0.1). Cells with fewer than 200 or more than 6,000 detected genes, or with mitochondrial transcript percentages exceeding 10%, were excluded. Data were normalized using the NormalizeData function. Datasets from different samples were then integrated by identifying anchors with FindIntegrationAnchors and applying IntegrateData in Seurat. Principal component analysis was used for dimensionality reduction.

Cells were clustered using graph-based clustering of the principal component analysis-reduced data with the Louvain algorithm after construction of a shared nearest-neighbor

graph. For subclustering, the same workflow—including scaling, dimensionality reduction, and clustering—was applied to selected data subsets, typically restricted to a single cell type.

For each cluster, differentially expressed genes (DEGs) were identified using the Wilcoxon rank-sum test between the two groups, with thresholds of $\log_2FC > 0.25$ and adjusted $p < 0.05$. The clusterProfiler package (v3.11) was used for Gene Ontology (GO) and Kyoto Encyclopedia of Genes and Genomes (KEGG) enrichment analyses, with adjusted $p < 0.05$ considered statistically significant. GO and KEGG term enrichment were assessed using the gseGO and gseKEGG functions in clusterProfiler, with a p-value threshold of 0.05.

Gene set variation analysis (GSVA) was performed using the GSVA package (v1.52.3) to assess mechanical stimulus–associated transcriptional programs. Cell-cycle scores were calculated using the CellCycleScoring function in Seurat based on the expression of S-phase and G2/M-phase marker genes. Individual cells were assigned to G1, S, or G2/M according to their scores. The proportion of cells in each phase was calculated separately for each sample to characterize cell-cycle distributions in the control and acupuncture groups.

Pseudotime analysis was performed with Slingshot version 2.2.1, with developmental trajectories inferred from cluster-specific DEGs. Cell–cell communication was analyzed using CellChat (v1.5.0). Communication networks were constructed by integrating the number and strength of interactions for each cluster. Dominant signal senders and receivers were visualized in two dimensions on the basis of the total outgoing and incoming communication probabilities for each cell cluster. Differences in the number and strength of interactions between the CG and AG communication networks were visualized as heatmaps.

2.6 Extraction and primary culture of TCs

TCs were extracted from the mouse dorsal midline Sf. Tissue samples were collected and processed following established protocols [19]. Sf was scraped under sterile conditions and digested with 2 mg/mL collagenase type IV (Solarbio, C8160, Beijing, China) at 37°C. The resulting suspension was sequentially passed through 100- and 40-μm cell strainers, followed by treatment with red blood cell lysis buffer (Biosharp, BL503A). The resulting cell suspension was plated in 6-well plate for 2 h to purify TCs and allow fibroblast attachment. Then, slowly adherent cells left on the plate surface were transferred to new culture plate. Isolated TCs were cultured in DMEM/F12

medium (Gibco, 11330032), supplemented with 10% FBS (FBS, Gibco, 10099141) and 1% penicillin–streptomycin (Solarbio, P7630). The cells were incubated in a 37°C incubator with 5% CO2. Immunofluorescence staining was performed to confirm the purity of the TC population.

2.7 Mechanical stretch *in vitro*

Recent advances in cellular mechanobiology have provided new insight into the mechanistic basis of acupuncture [20]. As a well-controlled mechanical stimulus, uniaxial stretching is widely used to interrogate force-sensitive cellular processes [21].

Isolated primary TCs were seeded in Matrigel-coated cell culture chambers and maintained at 37°C in a 5% CO_2 atmosphere. Mechanical strain was applied using a cell-stretching device (Cell Tank; Surface Force, Hangzhou, China). Cells were subjected to uniaxial cyclic stretch at 15% strain and 0.5 Hz with a sinusoidal waveform for 1, 3, or 6 h, consistent with previously reported protocols [22, 23]. Control cells were cultured in identical flexible chambers without mechanical stretching.

2.8 Transmission electron microscopy (TEM)

Skin and cell samples were fixed overnight in pre-cooled 2.5% glutaraldehyde prepared in 0.2 mol/L PBS and post-fixed in 1% osmium tetroxide for 1 h at 4°C. Samples were then dehydrated through a graded acetone series (30–100%) and embedded in Epon 812 resin. Ultrathin sections (70 nm) were double-stained with 1% uranyl acetate and lead citrate for 20 min and examined using a Hitachi HT7800 transmission electron microscope (Japan).

2.9 Scanning electron microscopy (SEM)

Samples were fixed overnight at 4°C in 2.5% glutaraldehyde prepared in 0.2 mol/L PBS and washed with ultrapure water. They were subsequently dehydrated through a graded ethanol series (50–100%), followed by solvent substitution with tert-butanol. After lyophilization, the samples were sputter-coated with gold and examined under a Hitachi Regulus 8100 scanning electron microscope (Japan).

2.10 Immunoelectron microscopy (IEM)

Cells were fixed in PBS containing 0.5% glutaraldehyde and 3% PFA for 1 h at 4°C and then blocked with 3% BSA for 30 min. The cells were incubated with an anti-CD34 primary antibody (1:100, Abclonal, A13929) for 3 h at 37°C. After washing with 1% BSA, samples were incubated for 1 h with the corresponding secondary antibody (1:50; goat anti-rabbit IgG conjugated to 35-nm colloidal gold particles; Solarbio, K1034G-G35). Subsequent processing was performed according to standard SEM protocols, and

samples were imaged using a Hitachi Regulus 8100 scanning electron microscope.

2.11 Cell cycle assay

Cell-cycle distribution was analyzed by flow cytometry after propidium iodide (PI) staining using a Cell Cycle Detection Kit (KGA9101-20, KeyGEN Biotech) according to the manufacturer's protocol. Cells were trypsinized, washed twice with PBS, and fixed overnight in 70% ethanol at −20°C. After washing with PBS, cells were stained with PI/RNase A for 60 min. Cell cycle distribution was acquired by flow cytometry (Beckman Coulter, CytoFlex, USA) and analyzed using FlowJo v10.8.1 software (FlowJo, LLC, Ashland, OR).

2.12 Scratch wound assay

Following mechanical stretching, confluent TC monolayers were scratched linearly with a sterile 200 μL pipette tip. The monolayers were immediately washed and incubated in Opti-MEM. Images of the wound area were acquired at 0, 12, and 24 h. Cell migration was quantified by assessing percentage wound closure using the ImageJ software.

2.13 Quantitative proteomic analysis

2.13.1 Sample Handling

Control and mechanically stretched TCs (four independent biological replicates per group) were harvested and lysed in buffer containing 8 M urea, 1 mM PMSF, and 2 mM EDTA. The supernatant was collected by centrifugation, and four volumes of cold acetone were added for overnight precipitation at −20 °C. The precipitate was washed three times with cold acetone and dissolved in 8 M urea. Total protein concentration was determined using a BCA assay kit. One hundred micrograms of protein was reduced with DTT (5 mM, 37 °C, 45 min), alkylated with iodoacetamide (11 mM, room temperature, dark, 15 min), and digested with trypsin overnight at 37 °C. The digested peptides were acidified with 20% TFA (pH 2–3), desalted with C18 resin, and quantified with the Pierce Quantitative Peptide Assay Kit.

2.13.2 LC–MS/MS analysis

Peptides were separated on a Vanquish Neo UHPLC system (Thermo Fisher Scientific) with a PepMap Neo trap column and an Easy-Spray PepMap Neo UHPLC column (150 μm × 15 cm, 2 μm), with 200 ng peptide injected per run and a flow rate of 2.5 μL/min. For data-independent acquisition (DIA) analysis, samples were analyzed on an Orbitrap Astral high-resolution mass spectrometer in positive ion mode: precursor scan range 380–980 m/z, MS1 resolution 240,000 at 200 m/z; MS2 acquired in DIA mode with

299 variable-width windows (HCD collision energy 25%).

2.13.3 Database search and quantification

Raw data were analyzed using DIA-NN (v1.8.1) in library-free mode. The UniProtKB mouse proteome database (uniprotkb_proteome_UP000000589_mouse_54910_20240528.fasta; 54,910 sequences) was used to generate a spectral library through neural network-based deep-learning algorithms. Four biological replicates were set per group. Differentially expressed proteins (DEPs) were defined by fold change >1.2 or < 0.83, and p -value < 0.05. Functional annotation and enrichment analyses (GO, KEGG, protein domain, subcellular localization, signal peptide) were performed, and PPI networks were constructed using the STRING database and visualized in Cytoscape (v3.9.1).

2.14 siRNA-mediated knockdown

Small interfering RNAs (siRNAs) targeting mouse ITGB1, a negative-control siRNA (NC siRNA), and siRNA-Mate Plus were purchased from GenePharma. At 60% confluence, TCs were transfected with ITGB1-targeting siRNAs (50 nM) or NC siRNA in Opti-MEM using siRNA-Mate Plus according to the manufacturer's instructions. Knockdown efficiency was assessed by qPCR and WB after 48 h. The siRNA sequences used in this study are listed in Table S1.

For functional analyses, TCs were assigned to four groups: (1) si-NC, (2) si-ITGB1, (3) si-NC + stretch, and (4) si-ITGB1 + stretch. Cells in the stretch groups were subjected to uniaxial cyclic stretch at 15% strain and 0.5 Hz for 6 h, whereas the corresponding non-stretched groups were maintained under otherwise identical culture conditions without mechanical stretch.

2.15 Transwell assay

Cell migration was assessed using 24-well Transwell inserts with an 8-μm pore size (Nest Biotechnology, Wuxi, China). Briefly, 600 μL of DMEM/F12 supplemented with 10% FBS was added to the lower compartment, whereas 4×10^4 TCs suspended in 200 μL of Opti-MEM (Gibco, 31985062) were seeded in the upper compartment following cyclic stretching. After 24 h, non-migrated cells remaining on the upper surface of the membrane were removed, whereas cells that had migrated to the underside were washed, fixed with 4% PFA, and stained with 0.1% crystal violet. Five fields in the central and peripheral regions of each membrane were randomly selected and imaged using the Olympus BX53 microscope. Cell numbers per field were quantified by ImageJ software (NIH).

2.16 Immunofluorescence (IF)

Skin sections were deparaffinized and subjected to heat-induced antigen retrieval. Cultured cells were fixed with 4% PFA for 15 min. Following permeabilization with 0.1% Triton X-100 in PBS, tissue sections or cell-containing slides were blocked with 5% bovine serum albumin (BSA, Boster, AR0004). Samples were incubated overnight at 4°C with primary antibodies against CD34 (1:200, Abclonal, A13929), PDGFRα (1:200, SantaCruz, sc-398206), YAP (1:100, Selleck, F0366), and Ki67 (1:1000, Proteintech, 28074-1-AP). Slides were incubated with CoraLite488-conjugated goat anti-rabbit IgG (1:200, proteintech, SA00013-2) and CoraLite594-conjugated goat anti-mouse IgG (1:200, proteintech, SA00013-3) secondary antibodies for 1 h at 37°C in the dark. F-actin was stained with rhodamine-labeled phalloidin (1:100, Abclonal, RM02835) diluted in 1% BSA and 0.1% Triton X-100. The samples were then counterstained with DAPI, mounted with an antifade reagent (Beyotime, P0126), and imaged with an Olympus BX53 microscope.

CD34/PDGFRα are the most commonly used marker combinations for TCs identification [24]. TC density was quantified following established protocols [19]. We counted cells co-expressing CD34 and PDGFRα, with a DAPI-positive nucleus and thin prolongations, per square millimeter of Sf. The cell area per μm², percentage of Ki67 positive cells, mitochondrial length, mitochondrial area per μm² and nuclear YAP localization (%) were quantified by ImageJ software.

2.17 qPCR

Total RNA was extracted from TCs with TRIzol and reverse-transcribed into cDNA with HiScript II Q RT SuperMix (Vazyme, Nanjing, China) according to the manufacturer's instructions. Quantitative real-time PCR was performed using ChamQ Universal SYBR qPCR Master Mix (Vazyme, Nanjing, China) on a CFX Connect Real-Time PCR Detection System (Bio-Rad). Each reaction was performed in triplicate. GAPDH served as the reference gene for data normalization. Relative gene expression was calculated using the $2^{-\Delta\Delta Ct}$ method. Primer sequences are provided in Table S2.

2.18 Western blotting (WB)

Following mechanical stretching, cells were lysed on ice in RIPA buffer (Beyotime, P0013B) supplemented with phosphatase and protease inhibitor cocktails (Beyotime, P1045) and centrifuged at 12,000 × g for 10 min. Protein concentrations were determined using a BCA protein assay kit (Beyotime, P0010S). Proteins were resolved on 10% SDS–PAGE gels and transferred onto methanol-activated polyvinylidene

fluoride membranes (Millipore, MA). Membranes were blocked with 5% skim milk in TBST for 2 h at room temperature and incubated overnight at 4°C with primary antibodies against ITGA5 (1:1000, Abclonal, A19069), ITGB1 (1:1000, Abclonal, A23497), CD34 (1:1000, Abclonal, A13929), PDGFRα (1:1000, SantaCruz, sc-398206), E-cadherin (1:500, SantaCruz, sc-8426), ROCK2 (1:10000, Selleck, F1209), FAK (1:1000, Huabio, ET1602-25), phospho-FAK (Tyr397) (1:500, Huabio, ET1610-34), YAP (1:1000, Selleck, F0366), phospho-YAP (Ser127) (1:1000, Huabio, ET1611-69), and GAPDH (1:1000, Affinity, AF7021). After washing with TBST, membranes were incubated for 1 h with HRP-conjugated goat anti-rabbit (1:5000, Zhongshan Golden Bridge, ZB2301) or goat anti-mouse (1:5000, Zhongshan Golden Bridge, ZB5305) secondary antibodies. Protein bands were visualized using a Tanon 5200 Multi imaging system (Tanon, Shanghai, China).

2.19 Statistical analysis

Data are presented as the mean ± standard error of the mean. Statistical analyses were performed using GraphPad Prism 8.3.0 (GraphPad Software, Inc.). Differences between two groups were assessed using an unpaired, two-tailed Student's t-test. Comparisons among three or more independent groups involving a single factor were performed using one-way analysis of variance (ANOVA), followed by Tukey's multiple comparisons test. For the siRNA functional experiments, two-way ANOVA was used to assess the effects of siRNA treatment (si-NC versus si-ITGB1), mechanical stretch (unstretched versus stretched), and their interaction, followed by Tukey's multiple comparisons test. Statistical significance was defined as $p < 0.05$ and denoted as follows: *$p < 0.05$, **$p < 0.01$, ***$p < 0.001$, and ****$p < 0.0001$.

3 Results

3.1 CPTCs exhibited distinctive mechanical stimulus response signatures in the mouse dorsal midline Sf

To characterize TCs in the dorsal midline Sf, we combined histological and IF analyses with electron microscopy and scRNA-seq (Figure 1A). H&E staining delineated the subcutaneous fascia beneath the dermis (Figure 1B). IF revealed numerous elongated $CD34^+/PDGFR\alpha^+$ TCs within this layer (Figure 1C). TEM confirmed the presence of TCs by demonstrating their characteristic slender and long telopodes (Figure 1D). Interestingly, SEM revealed that fascial TCs exhibited a broad, flattened, membranous morphology, with thin extensions spreading over and between collagen bundles (Figure

1E). This flattened morphology was further corroborated by laminar isolated TCs *in vitro* under SEM (Figure S1A). Cultured TCs exhibited co-expression of CD34 and PDGFRα, with immunogold labeling demonstrating CD34 expression on their surfaces (Figure S1B, C).

Unsupervised clustering and annotation using canonical lineage markers identified 10 cell populations: $CD34^{+}$/$PDGFR\alpha^{+}$ TCs (CPTCs), fibroblasts, endothelial cells, macrophages, satellite cells, mast cells, T cells, mural cells, skeletal muscle cells (SMCs), and Schwann cells (Figure 1F). Cell-type annotations were supported by characteristic marker expression, including *Cd34* and *Pdgfra* in CPTCs (Figure 1G). CPTCs constituted the predominant population among the profiled cells (Figure 1H).

We next examined transcriptional signatures associated with mechanical responsiveness. CPTCs exhibited the highest standardized GSVA scores for "response to mechanical stimulus" and "cellular response to mechanical stimulus", with Z-scores of 1.91 and 1.43, respectively (Figure 1I). Heatmap analysis highlighted the expression of genes involved in extracellular matrix remodeling (*Mmp14*, *Mmp2*, and *Postn*), cell–matrix adhesion (*Itga2*), stress signaling (*Mapk9*), and transcriptional regulation (*Hdac4*) in CPTCs (Figure 1J). GSEA comparing CPTCs with the remaining cell populations revealed positive enrichment of extracellular matrix assembly (Figure 1K). TEM revealed focal adhesion structures at the interface between CPTC processes and the surrounding extracellular matrix (Figure 1L).

CellChat analysis further predicted extensive communication between CPTCs and other fascial cell populations. TEM showed that TC processes were closely apposed to macrophages, fibroblasts, and mast cells, demonstrating their intimate spatial relationships with neighboring cells (Figure S1D). CPTC outgoing signaling included prominent extracellular matrix-associated pathways, notably COLLAGEN, LAMININ, FN1, and TENASCIN (Figure S1E). At the ligand–receptor level, Col1a1–Cd44 was a prominent predicted interaction connecting CPTCs to fibroblasts, macrophages, satellite cells, mast cells, and T cells, as well as to CPTCs themselves (Figure S1F).

3.2 Needle manipulation induced mechanical coupling between CPTCs and collagen fibers

To delineate the structural relationship between CPTCs and the fascial extracellular matrix, we examined their spatial association with collagen fibers. TEM revealed three spatial relationships between CPTCs and collagen bundles: the slender processes wrapping around bundles, intercalating between adjacent bundles, or closely adhering

to one side. Consistent with these findings, SEM showed flattened CPTCs arranged around and among collagen fibers (Figure S2), highlighting their intimate structural association with the collagenous matrix.

We next examined tissue retrieved immediately after a single session of needle manipulation involving lifting–thrusting and rotation at GV14 or GV4 (Figure 2A). SEM revealed tissue wrapped around the needle shaft, with a densely interwoven collagen fiber network visible at higher magnification (Figure 2B, C). Notably, sheet-like CPTCs were embedded within the densely interwoven collagen fiber network. Under the mechanical constraints imposed by the surrounding collagen matrix, CPTCs displayed a taut membranous morphology (Figure 2D, d).

Specimens detached from the needles retained a hollow tubular architecture (Figure 2E). Masson's trichrome staining demonstrated collagen-rich tissue containing muscle fibers from the panniculus carnosus (Figure 2F). TEM identified slender CPTC processes interspersed among collagen fibers, accompanied by IF, which further revealed elongated $CD34^{+}$/PDGFRα+ TCs within the tubular tissue wall (Figure 2G, H).

3.3 Acupuncture increased CPTC abundance and enhanced transcriptional signatures of proliferation and mechanical responses

To characterize the responses of fascial CPTCs to acupuncture, mice received daily needle stimulation for 7 days, followed by scRNA-seq and morphological analyses (Figure 3A). t-SNE visualization identified ten major cell populations in both groups (Figure 3B). CPTCs remained the predominant population, with their proportion among the profiled cells increasing from 76.03% in the control group (CG) to 82.49% in the acupuncture group (AG) (Figure 3C). Cell-cycle analysis revealed higher proportions of CPTCs assigned to S and G2/M phases in both AG samples, accompanied by a reduction in the G1 fraction (Figure 3D). Consistently, GSEA demonstrated significant positive enrichment of the DNA replication gene set in AG CPTCs (NES = 1.521, P = 0.004; Figure 3E), supporting enhanced proliferation-associated transcriptional activity. These findings were validated by CD34/PDGFRα immunostaining and TEM. IF demonstrated a significantly greater density of CPTCs per mm^2 in the Sf of AG mice than in that of CG mice ($P < 0.0001$; Figure 3F, J). TEM further revealed a significant increase in slender TC projections in the AG group (Figure 3G).

CellChat analysis further showed that acupuncture increased the interaction strength between CPTCs and other cell types (Figure 3H). GO analysis of genes upregulated in CPTCs highlighted enrichment of terms related to mechanical stimulus responses (*Fos*,

Txnip, *Irf1*, and *Bnip3*), positive regulation of actin filament bundle assembly (*Ccn2*, *Pfn1*, and *Sdc4*), focal adhesion assembly (*Taok2* and *Cttn*), and extracellular matrix assembly (*Efemp2* and *Smpd3*) (Figure 3I, Table S3). GSEA additionally revealed significant positive enrichment of gene sets related to adherens junctions, Hippo signaling, and protein processing in the endoplasmic reticulum (Figure 3K, Table S4).

3.4 Acupuncture enhanced stress-response programs in CPTC-C1 subpopulation and adhesion–cytoskeletal signatures in CPTC-C4 subcluster

To resolve CPTC heterogeneity, we identified five transcriptionally distinct subpopulations, designated CPTC-C0–CPTC-C4 (Figure 4A). Among these, CPTC-C1 and CPTC-C4 displayed molecular features relevant to stimulus responses and cell–matrix interactions. CPTC-C1 showed high expressed of *Fos* and *Jun*, which encode two major components of the AP-1 transcription factor complex. CPTC-C4 was characterized by high expression of *Thy1* (Figure 4B; Figure S3A), a cell-surface glycoprotein that modulates integrin-dependent mechanotransduction.

GO enrichment analysis of subpopulation-enriched marker genes further supported these functional distinctions. CPTC-C1 was enriched for cellular stress responses and CPTC-C4 showed enrichment for extracellular matrix organization, cell adhesion, and actin filament bundle assembly. The remaining subpopulations exhibited signatures associated with cytokine responses and immune regulation in CPTC-C0, cell migration and vesicle-mediated transport in CPTC-C2, and translation and ribosome biogenesis in CPTC-C3 (Figure S3B). Following acupuncture, the proportions of CPTC-C1 and CPTC-C4 increased from 11.25% to 20.14% and from 0.83% to 1.65%, respectively (Figure 4C). CPTC-C1 showed 1,828 upregulated and 419 downregulated genes in AG versus CG, with increased expression of *Atf3*, *Fos*, *Jun*, and *Hspa1a* (Figure 4D). With CPTC-C2 designated as the root, the displayed Slingshot-inferred trajectory traversed the CPTC-C1 and CPTC-C0 regions and extended toward CPTC-C4 (Figure 4E). The RNA velocity–derived differentiation vector field showed a concordant directional flow, supporting the predicted ordering of these states (Figure 4F).

We next assessed the mechanical-response signatures in CPTC subpopulations. CPTC-C4 exhibited the highest standardized scores for the “response to mechanical stimulus” gene set (Figure 4G). Notably, examination of genes associated with mechanosensing and mechanotransduction, including *Piezo1*, *Trpv4*, *Itga5*, and *Itgb1*, revealed broad expression of *Itgb1* in CPTC-C4 (Figure 4H). CPTC-C4 showed 279 upregulated and 58 downregulated genes in AG versus CG, including upregulation of genes associated

with matrix adhesion (*Fn1*) and actin organization (*Fscn1*, *Actn4*, and *Actn1*) (Figure 4I). SEM revealed a highly developed microfilament cytoskeletal network in CPTCs (Figure S3C). Consistently, KEGG enrichment analysis of the upregulated genes identified ECM–receptor interaction, focal adhesion, and regulation of actin cytoskeleton as enriched pathways (Figure 4J, Table S5). GSEA further revealed activation of these pathways in CPTC-C4 from AG relative to CG (Figure 4K, Table S6).

3.5 Acupuncture strengthened predicted fibronectin–integrin α5β1 signaling to CPTC-C4

To investigate intercellular signaling associated with CPTC subcluster responses to acupuncture, we compared cell–cell communication networks between AG and CG using CellChat. Differential interaction analysis highlighted CPTC-C4 as a prominent signaling sender and receiver, with increased incoming signaling strength and the largest increase in total outgoing signaling strength among all cell populations in AG relative to CG (Figure S4A, B). CellChat analysis revealed a widespread increase in both the number and strength of predicted interactions among CPTC subpopulations following acupuncture (Figure S4C).

At the ligand–receptor level, predicted Fn1–(Itga5+Itgb1) communication from each CPTC subpopulation to CPTC-C4 was significantly enhanced in AG relative to CG (Figure S4D). NicheNet analysis, with CPTC-C0–CPTC-C3 as candidate senders and CPTC-C4 as the receiver, further revealed that *Cxcl12* ranked highest in predicted ligand activity, and ligand–target analysis identified *Gsn* (encoding the actin-regulatory protein gelsolin) among its predicted downstream targets in CPTC-C4 (Figure S4E).

3.6 Cyclic mechanical stretch triggered functional activation and ultrastructural remodeling of CPTCs

To examine the functional responses of CPTCs to mechanical stimulation, primary cultured CPTCs were subjected to cyclic stretch at 15% strain and 0.5 Hz for 1, 3, or 6 h, with static cultures serving as controls (Figure 5A). Stretched CPTCs tended to align perpendicular to the stretching direction, particularly at 6 h (Figure 5B). WB showed significantly increased CD34 and PDGFRα protein levels after 6 h of stretch (Figure 5C, E). This time point was used for subsequent functional analyses. Cell-cycle analysis revealed a significant decrease in the G1-phase fraction and an increase in the S-phase fraction following stretch (Figure 5D, E). Consistently, the proportion of $Ki67^{+}$ CPTCs increased significantly, supporting enhanced proliferative activity (Figure 5F, J).

Phalloidin staining further revealed F-actin reorganization, with more aligned filament bundles and a significantly increased cell spreading area (Figure 5G, J). To assess whether these responses were accompanied by altered migration, CPTCs were subjected to scratch-wound and Transwell assays after 6 h of stretch. Stretch intervention significantly increased wound closure at both 12 and 24 h and the number of CPTCs migrating through Transwell membranes at 24 h (Figure 5H–J).

To further characterize the structural changes accompanying these functional responses, CPTCs were examined by TEM. Compared with static controls, stretched CPTCs exhibited more elongated cell profiles and elongated mitochondria. Morphometric analysis confirmed significant increases in both the cross-sectional area and length of mitochondria in stretched CPTCs. More numerous membrane-associated caveolae and dilated rough endoplasmic reticulum cisternae were also observed in stretched CPTCs (Figure S5).

3.7 Mechanical stretch elicited changes in ITGB1–FAK–ROCK2 signaling and promoted YAP nuclear accumulation in CPTCs

To investigate the molecular responses underlying stretch-induced changes in CPTCs, proteomic profiles were compared between cells subjected to 6 h of cyclic stretch and static controls. 230 DEPs were identified, comprising 107 upregulated and 123 downregulated proteins. Upregulated proteins included RAC1, ROCK2, and JUN (Figure 6A). Predicted subcellular localization assigned the largest proportions of DEPs to the nucleus (33.48%), cytoplasm (24.35%), and extracellular compartment (16.09%) (Figure 6B). GO classification linked these proteins to stimulus responses, signaling, transcriptional regulation, and protein-folding functions (Figure 6C, Table S7).

KEGG highlighted the enrichment of focal adhesion and adherens junction in stretched CPTCs (Figure 6D, Table S8). HSPA1A, HSPA1B, HSPA1L, and HSPB1 were significantly upregulated (Figure 6E). Consistently, GSEA showed positive enrichment of “heat shock protein binding” (NES = 1.837) and “ATP-dependent protein folding chaperone” (NES = 1.898) (Figure 6F). SEM showed that stretched CPTCs exhibited reinforced intercellular adherens junctions and strengthened focal adhesions (Figure 6G), aligned with KEGG analysis.

WB further showed that ITGB1 protein levels increased significantly at 1 and 6 h. At 6 h, the p-FAK (Tyr397)/FAK ratio, ROCK2, and E-cadherin expression were significantly increased (Figure 6H). We next investigated YAP, a canonical mechanosensitive transcriptional coactivator [25]. WB showed decreased ratios of p-YAP

(Ser127)/YAP in stretched CPTCs at 6 h, accompanied by enhanced nuclear accumulation of YAP by IF staining (Figure 6H, I). Ultrastructural analysis revealed a marked reduction in perinuclear heterochromatin after 6 h of stretching (Figure 6J). A PPI network constructed from the four candidate proteins ITGB1, FAK, ROCK2, and YAP showed functional associations among them (Figure 6K).

3.8 ITGB1 was required for mechanical stretch-induced mechanotransduction in CPTCs

To examine the functional contribution of ITGB1 to CPTC responses to mechanical stretch, four siRNAs targeting *Itgb1* were evaluated. All four reduced *Itgb1* mRNA and ITGB1 protein levels relative to the negative control siRNA (si-NC). Among them, si-ITGB1-2 achieved the greatest silencing efficiency and was selected for subsequent functional assays (Figure 7A). Stretch significantly increased the proportion of $Ki67^+$ CPTCs in the si-NC group compared with static controls, whereas ITGB1 knockdown significantly reduced this proportion under mechanical stretching compared with si-NC controls (Figure 7B, G). Transwell assays showed a corresponding effect on migration: ITGB1 knockdown markedly attenuated stretch-induced enhancement of CPTC migration (Figure 7C, G).

WB confirmed reduced ITGB1 protein levels after knockdown under both static and stretching conditions. Compared with stretched si-NC controls, ITGB1 knockdown significantly reduced FAK phosphorylation and ROCK2 expression in stretched CPTCs (Figure 7D, G). ITGB1 knockdown attenuated stretch-induced YAP dephosphorylation (Figure 7E, G). Consistently, immunofluorescence showed reduced nuclear YAP accumulation in stretched CPTCs after ITGB1 knockdown (Figure 7F).

4 Discussion

Collagen winding and extracellular matrix deformation form the biomechanical basis of the therapeutic efficacy of acupuncture [8, 9]. Whereas, the early mechanosensing cells during acupuncture manipulation have remained unclear. This study supports CPTCs as candidate initial mechanosensors linking physical needling to local biological responses. Their close association with collagen fibers and identification in needle-adherent tissue provide a structural basis for sensing needle-transmitted forces. CPTCs represented the predominant cell population in the dorsal midline Sf and exhibited remarkable responsiveness to mechanical stimulus. Moreover, functional experiments demonstrated increased cytoskeletal remodeling and CPTC proliferation following both manual acupuncture *in vivo* and cyclic stretch *in vitro*, indicating that CPTCs are

capable of mechanotransduction upon receiving mechanical signals from the collagen matrix.

Cells sense and respond to different types of mechanical cues through various mechanisms, including mechanosensitive ion channels, integrins, and the glycocalyx [26-29]. As transmembrane adhesion receptors, integrins bind the extracellular matrix and couple it to the actin cytoskeleton through focal-adhesion complexes, establishing an ECM–integrin–cytoskeleton system for force transmission and mechanotransduction [30, 31]. Single-cell profiling demonstrated distinct transcriptional characteristics of CPTC subpopulations in response to acupuncture. CPTC-C1 displayed an immediate-early and stress-related program characterized by *Fos*, *Jun* and *Atf3*, consistent with the AP-1/Hsp70-associated response reported by Huang et al. [15] in fascial CPTCs following acupuncture. Notably, CPTC-C4 exhibited the highest z-score for the "response to mechanical stimulus" among the five CPTC subclusters. In our study, high expression of *Itgb1* in CPTC-C4, together with enrichment of focal adhesion and actin-regulatory programs and enhanced Fn1–(Itga5+Itgb1) interactions, pointed to integrin-mediated mechanosensing.

ScRNA-seq analysis was further validated by cyclic-stretch experiments, which revealed increased ITGB1 protein abundance and signaling responses involving the ITGB1–FAK–ROCK2 axis. In agreement with our findings, Zhang et al. reported that mechanical stimuli activated a similar integrin–FAK signaling in periodontal ligament stem cells [32]. It is worth noting that ITGB1 silencing markedly attenuated stretch-induced downstream signaling and the associated proliferative and migratory responses, underscoring the indispensable role of ITGB1 in CPTC mechanotransduction. This interpretation of our findings is supported by a previous study in dermal fibroblasts, where Wen et al. demonstrated that β1-integrin blockade suppressed cyclic-strain-induced reorientation and FAK/Rho activation [33].

In CPTCs, ITGB1-mediated mechanotransduction was accompanied by cytoskeletal remodeling. Consistent with our findings, Langevin et al. demonstrated that acupuncture needle rotation induced fibroblast spreading and cytoskeletal reorganization [34]. Beyond these changes, stretched CPTCs exhibited ultrastructural remodeling, including mitochondrial elongation, dilation of rough endoplasmic reticulum cisternae, and increased caveolar abundance. Proteomic analysis further revealed upregulation of HSP70 family members and enrichment of ATP-dependent protein-folding chaperone functions. Together, these observations suggest that CPTCs

accommodate mechanical loading through structural reorganization and proteostatic adjustment [35-37], potentially helping to meet the energetic and biosynthetic demands associated with sustained mechanotransduction.

YAP, a key mechanosensitive transcriptional coactivator [25, 38], may provide a transcriptional link between ITGB1–FAK–ROCK2 signaling and the proliferative and cytoskeletal responses of CPTCs. Nuclear YAP cooperates with TEAD transcription factors to regulate gene programs involved in cell proliferation and cytoskeletal organization [39]. In the present study, uniaxial stretching promoted YAP nuclear accumulation in CPTCs, consistent with observations in MCF10A human mammary epithelial cells subjected to cyclic stretch [40]. Ultrastructural analysis additionally revealed reduced heterochromatin at the nuclear periphery, compatible with chromatin remodeling previously associated with nuclear softening under mechanical stress [41, 42]. Such nuclear remodeling may reduce mechanical resistance to nuclear entry, thereby facilitating YAP translocation and activation in CPTCs.

Previous studies have implicated fibroblasts [34, 43], mast cells [44], and macrophages [20] in responses to acupuncture-induced mechanical stimulation. Our findings suggest that CPTCs may participate in coordinating this multicellular response. Their spatial proximity to these cell populations and extensive predicted signaling interactions suggest opportunities for local intercellular communication. Specifically, CellChat predicted Col1a1–Cd44 interactions from CPTCs to all three populations, placing CPTCs within a shared matrix-associated communication network. This interaction is supported by studies demonstrating the immunomodulatory potential of CPTC–macrophage crosstalk. Huang et al. [13] reported that CPTCs modulated fascial macrophage states and reduced macrophage sensitivity to lipopolysaccharide, while Zhang et al. [14] linked Ptgs2^{+} CPTCs to M2 macrophage activation and anti-inflammatory responses.

5 Conclusions

In summary, we delineate a model of CPTC-mediated mechanotransduction during acupuncture (Figure 8), positioning CPTCs as candidate initial mechanosensors linking physical needling to local biological responses. Their close association with collagen fibers and presence in needle-adherent tissue support mechanical coupling with the matrix and provide a structural basis for sensing needle-transmitted forces. The *in vivo* and *in vitro* findings support mechanical activation of CPTCs, involving enhanced

proliferative responses, cytoskeletal remodeling, and intercellular communication. Single-cell analysis reveals heterogeneous CPTC responses: CPTC-C1 displays an immediate-early stress-response program, whereas CPTC-C4 exhibits enhanced adhesion–cytoskeletal programs. CPTC-C4 exhibited the remarkably high responsiveness to mechanical stimulus and high *Itgb1* expression. Together with enhanced predicted fibronectin–integrin α5β1 signaling to CPTC-C4, these features indicate a pivotal role for the ECM–integrin–cytoskeleton axis in mechanosensing. Moreover, cyclic stretch reveals an ITGB1-dependent mechanism involving FAK–ROCK2 signaling and YAP nuclear accumulation in stretch-induced CPTC proliferation, migration, and cytoskeleton remodeling. These findings suggest that ITGB1-dependent mechanotransduction contributes to the initiation of CPTC responses to physical needling. Activated CPTCs may subsequently engage neighboring cells and influence downstream local biological processes.

Declarations

Ethics approval

All animal experiments were approved by the Animal Welfare and Ethics Committee of Nanjing Agricultural University (approval no. NJAU.No20240102001).

Availability of data

The single-cell RNA-sequencing data are publicly available in the Gene Expression Omnibus under accession number GSE330613. Additional data supporting the findings of this study are available from the corresponding author upon reasonable request.

Competing interests

The authors declare no competing interests.

Funding

This work was supported by the National Natural Science Foundation of China (grant 31872433).

Author contributions

M.L. and C.Q.S. conceived and designed the study; M.L. and D.M. performed the experiments and analyzed the data; M.L. interpreted the experimental results, prepared the figures, and drafted the manuscript; Z.Z.W., H.H.X., Y.J.M., and C.Q.S. provided technical assistance and revised the manuscript.

Consent for publication

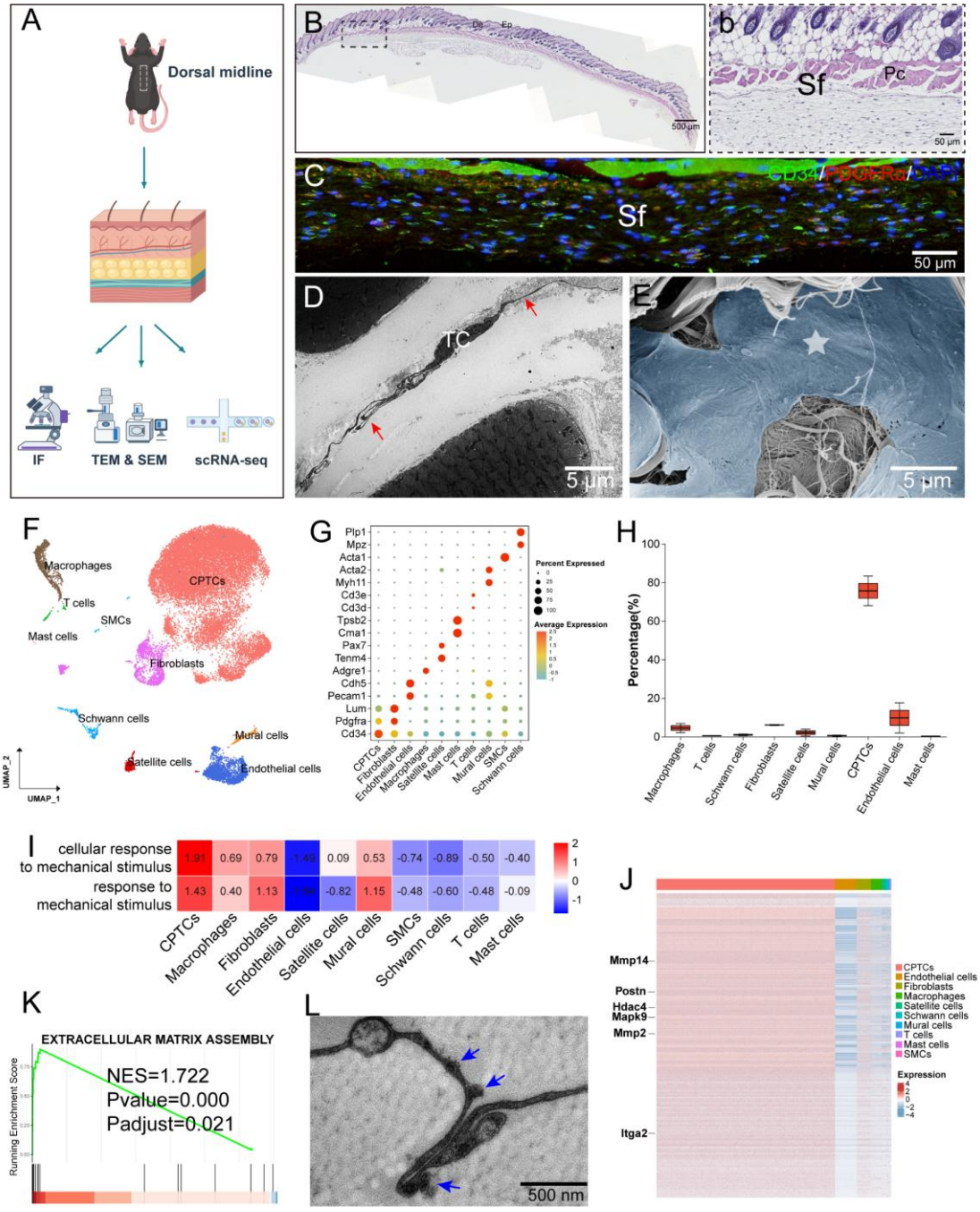
All authors reviewed and approved the final manuscript for publication.

Acknowledgements

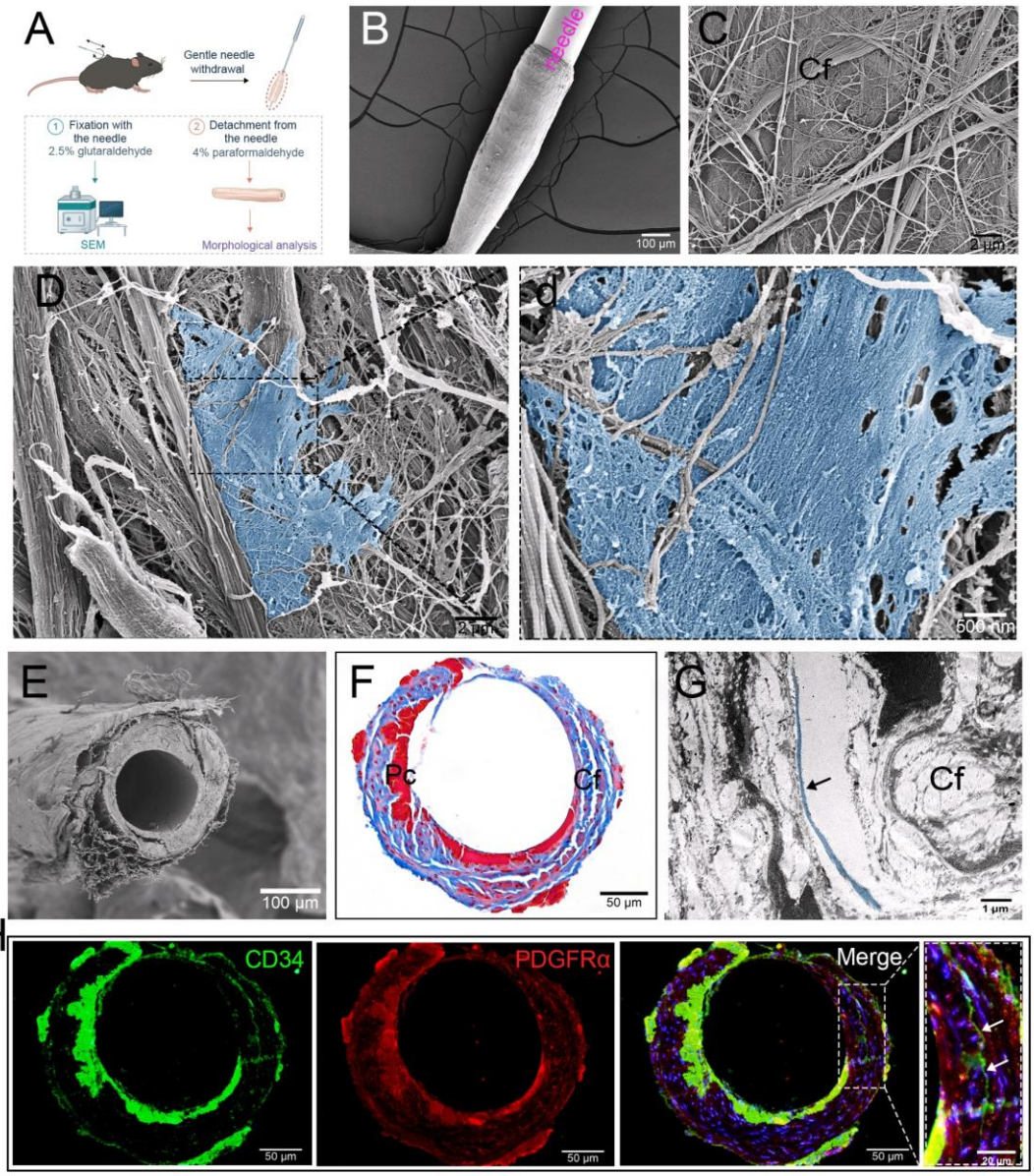
The authors gratefully acknowledge Professor He and Professor Wang at the State Key Laboratory of Crop Genetics & Germplasm Enhancement, Nanjing Agricultural University, for providing technical support for electron microscopy. The authors are also grateful to those who assisted in proteomic analysis at Wuhan Metware Biotechnology Co., Ltd.

Figures

Figure 1



692 **Figure 2**



693
694

Figure 3

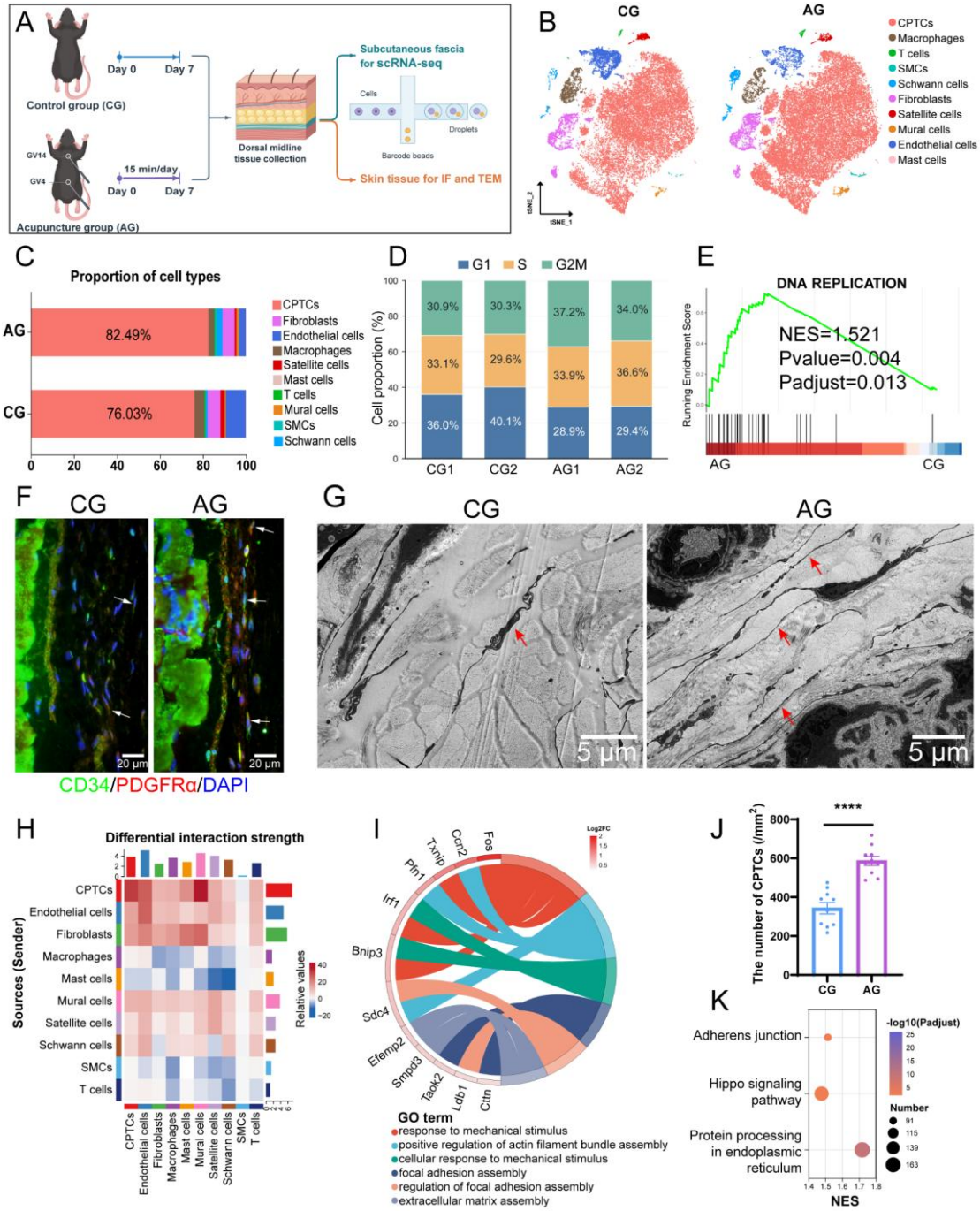

A
Control group (CG)
Day 0
Day 7
Acupuncture group (AG)
GV14
GV4
15 min/day
Dorsal midline tissue collection
Subcutaneous fascia for scRNA-seq
Skin tissue for IF and TEM
Cells
Droplets
Barcode beads
B
CG
AG
CPTCs
Macrophages
T cells
SMCs
Schwann cells
Fibroblasts
Satellite cells
Mural cells
Endothelial cells
Mast cells
C
Proportion of cell types
82.49%
76.03%
D
G1
S
G2M
Cell proportion (%)
30.9%
33.1%
36.0%
30.3%
29.6%
40.1%
37.2%
33.9%
28.9%
34.0%
36.6%
29.4%
CG1
CG2
AG1
AG2
E
DNA REPLICATION
NES=1.521
Pvalue=0.004
Padjust=0.013
Running Enrichment Score
F
CD34/PDGFRα/DAPI
20 μm
G
5 μm
H
Differential interaction strength
Sources (Sender)
Relative values
I
Log2FC
Fos
Con2
Txnip
Pfn1
Irf1
Bnip3
Sdc4
Efemp2
Smpd3
Tadk2
Ldb1
Cttn
GO term
response to mechanical stimulus
positive regulation of actin filament bundle assembly
cellular response to mechanical stimulus
focal adhesion assembly
regulation of focal adhesion assembly
extracellular matrix assembly
J
****
The number of CPTCs (/mm²)
K
Adherens junction
Hippo signaling pathway
Protein processing in endoplasmic reticulum
-log10(Padjust)
Number
NES

Figure 4

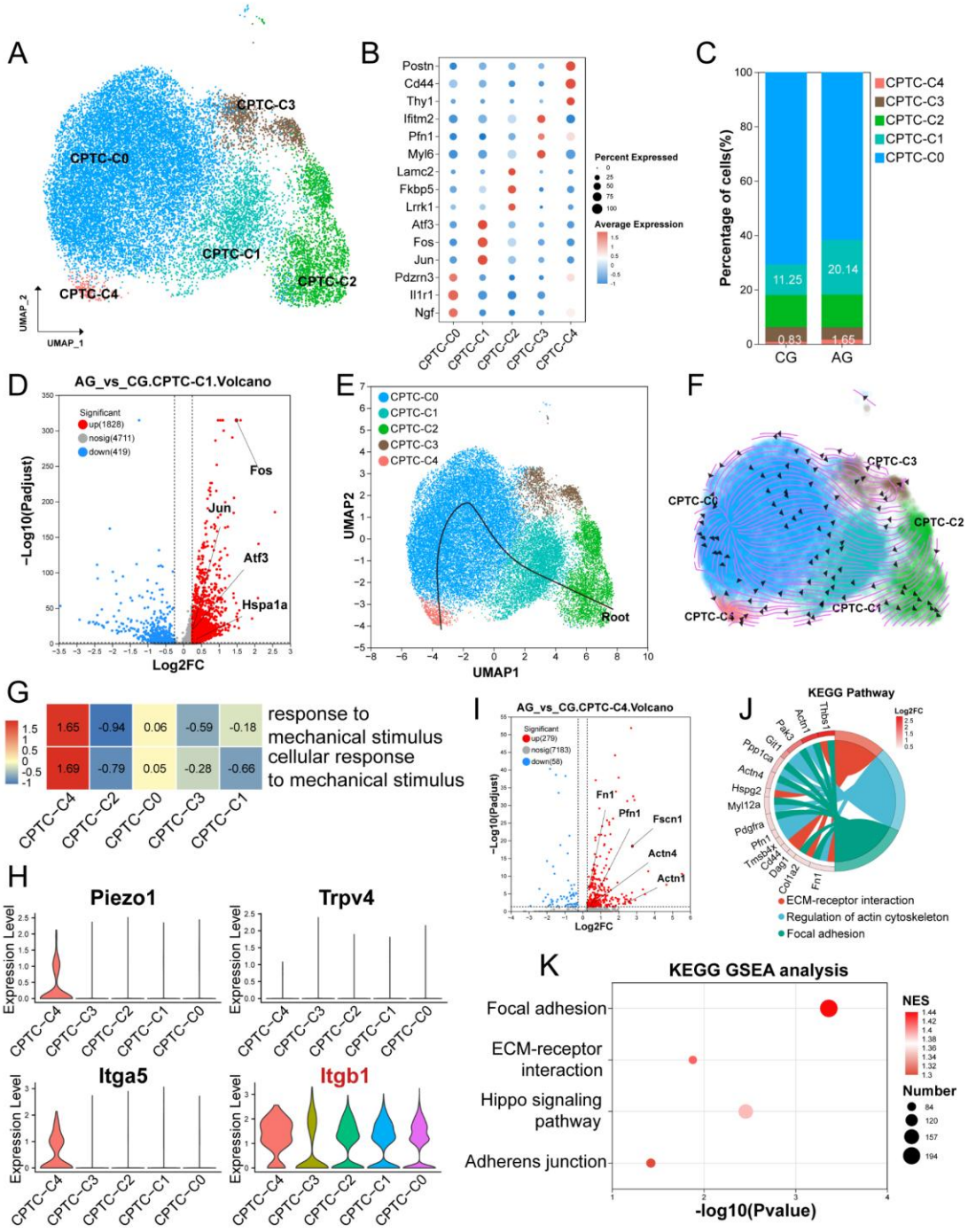

A
CPTC-C0
CPTC-C3
CPTC-C1
CPTC-C2
CPTC-C4
UMAP_2
UMAP_1
B
Postn
Cd44
Thy1
Ifitm2
Pfn1
Myl6
Lamc2
Fkbp5
Lrrk1
Atf3
Fos
Jun
Pdzrn3
Il1r1
Ngf
Percent Expressed
Average Expression
C
Percentage of cells(%)
11.25
20.14
0.83
1.65
CG
AG
D
AG_vs_CG.CPTC-C1.Volcano
Significant
up(1828)
nosig(4711)
down(419)
-Log10(Padjust)
Log2FC
Fos
Jun
Atf3
Hspa1a
E
UMAP2
UMAP1
Root
F
G
response to mechanical stimulus
cellular response to mechanical stimulus
1.65
-0.94
0.06
-0.59
-0.18
1.69
-0.79
0.05
-0.28
-0.66
H
Piezo1
Trpv4
Itga5
Itgb1
Expression Level
I
AG_vs_CG.CPTC-C4.Volcano
Significant
up(279)
nosig(7183)
down(58)
Fn1
Pfn1
Fscn1
Actn4
Actn1
J
KEGG Pathway
Log2FC
ECM-receptor interaction
Regulation of actin cytoskeleton
Focal adhesion
K
KEGG GSEA analysis
Focal adhesion
ECM-receptor interaction
Hippo signaling pathway
Adherens junction
NES
Number
-log10(Pvalue)

Figure 5

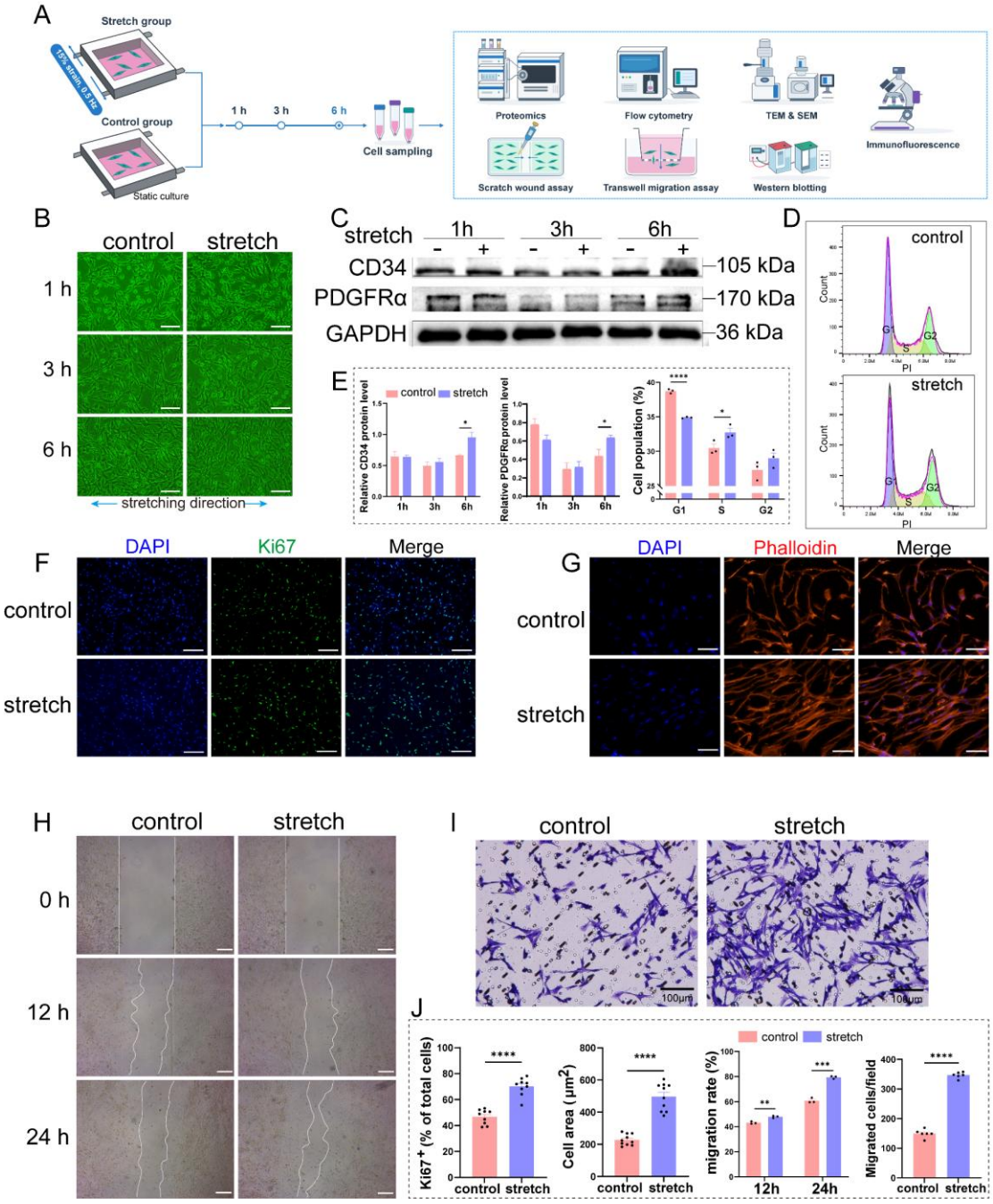

A
Stretch group
15% Strain, 0.5 Hz
Control group
Static culture
1 h
3 h
6 h
Cell sampling
Proteomics
Flow cytometry
TEM & SEM
Immunofluorescence
Scratch wound assay
Transwell migration assay
Western blotting
B
control
stretch
1 h
3 h
6 h
stretching direction
C
stretch
1h
3h
6h
CD34
PDGFRα
GAPDH
105 kDa
170 kDa
36 kDa
D
control
stretch
Count
PI
E
control
stretch
Relative CD34 protein level
Relative PDGFRα protein level
Cell population (%)
G1
S
G2
F
DAPI
Ki67
Merge
control
stretch
G
DAPI
Phalloidin
Merge
control
stretch
H
control
stretch
0 h
12 h
24 h
I
control
stretch
100μm
J
Ki67+ (% of total cells)
Cell area (μm2)
migration rate (%)
Migrated cells/field
control
stretch
12h
24h

Figure 6

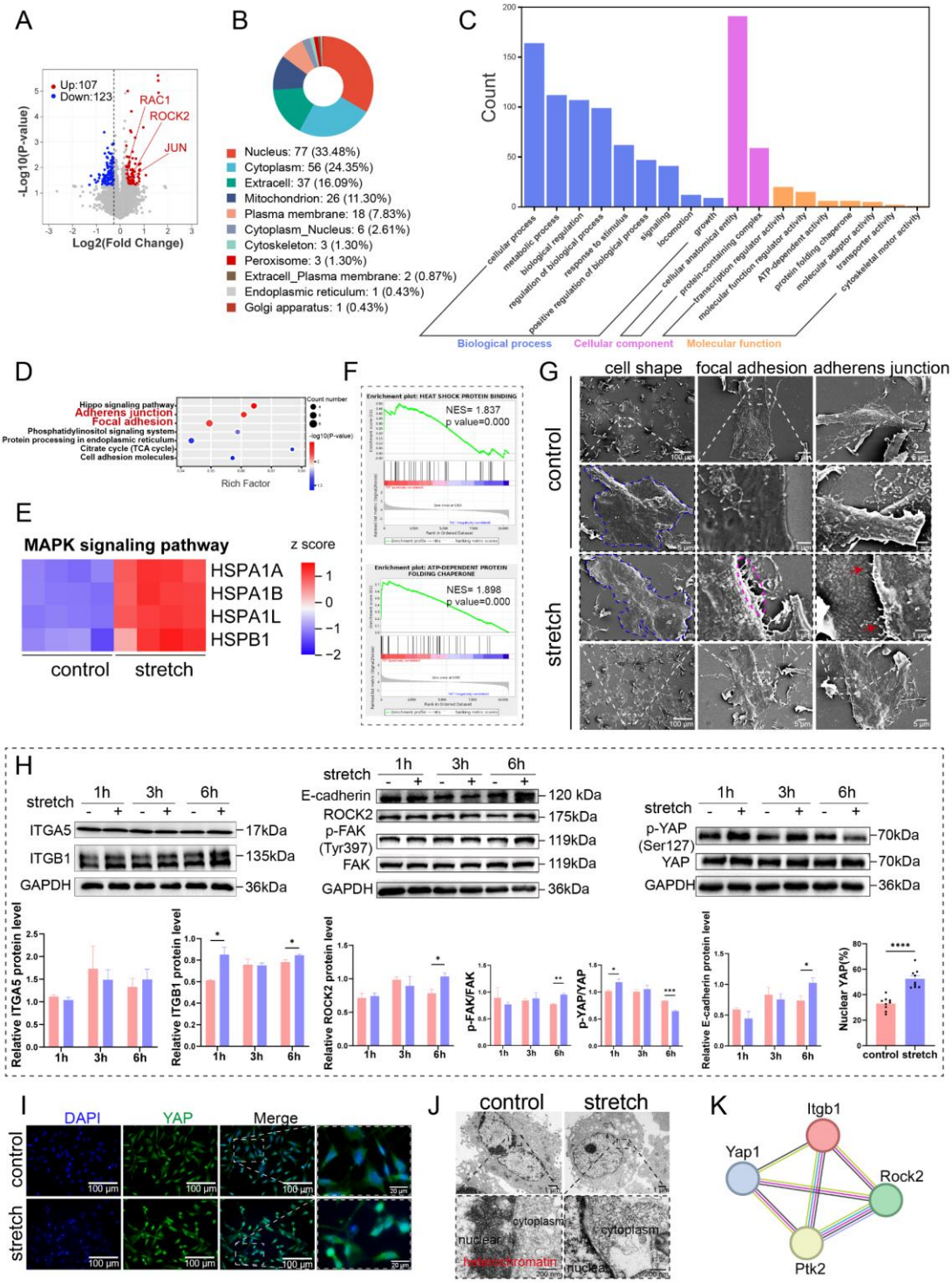

A
Up:107
Down:123
RAC1
ROCK2
JUN
-Log10(P-value)
Log2(Fold Change)
B
Nucleus: 77 (33.48%)
Cytoplasm: 56 (24.35%)
Extracell: 37 (16.09%)
Mitochondrion: 26 (11.30%)
Plasma membrane: 18 (7.83%)
Cytoplasm_Nucleus: 6 (2.61%)
Cytoskeleton: 3 (1.30%)
Peroxisome: 3 (1.30%)
Extracell_Plasma membrane: 2 (0.87%)
Endoplasmic reticulum: 1 (0.43%)
Golgi apparatus: 1 (0.43%)
C
Count
Biological process
Cellular component
Molecular function
D
Hippo signaling pathway
Adherens junction
Focal adhesion
Phosphatidylinositol signaling system
Protein processing in endoplasmic reticulum
Citrate cycle (TCA cycle)
Cell adhesion molecules
Rich Factor
E
MAPK signaling pathway
z score
HSPA1A
HSPA1B
HSPA1L
HSPB1
control
stretch
F
Enrichment plot: HEAT SHOCK PROTEIN BINDING
NES= 1.837
p value=0.000
Enrichment plot: ATP-DEPENDENT PROTEIN FOLDING CHAPERONE
NES= 1.898
p value=0.000
G
cell shape
focal adhesion
adherens junction
control
stretch
H
stretch
1h
3h
6h
ITGA5
17kDa
ITGB1
135kDa
GAPDH
36kDa
E-cadherin
120 kDa
ROCK2
175kDa
p-FAK (Tyr397)
119kDa
FAK
119kDa
p-YAP (Ser127)
70kDa
YAP
70kDa
Relative ITGA5 protein level
Relative ITGB1 protein level
Relative ROCK2 protein level
p-FAK/FAK
p-YAP/YAP
Relative E-cadherin protein level
Nuclear YAP(%)
control
stretch
I
DAPI
YAP
Merge
control
stretch
100 μm
20 μm
J
control
stretch
cytoplasm
nuclear
heterochromatin
K
Itgb1
Yap1
Rock2
Ptk2

Figure 7

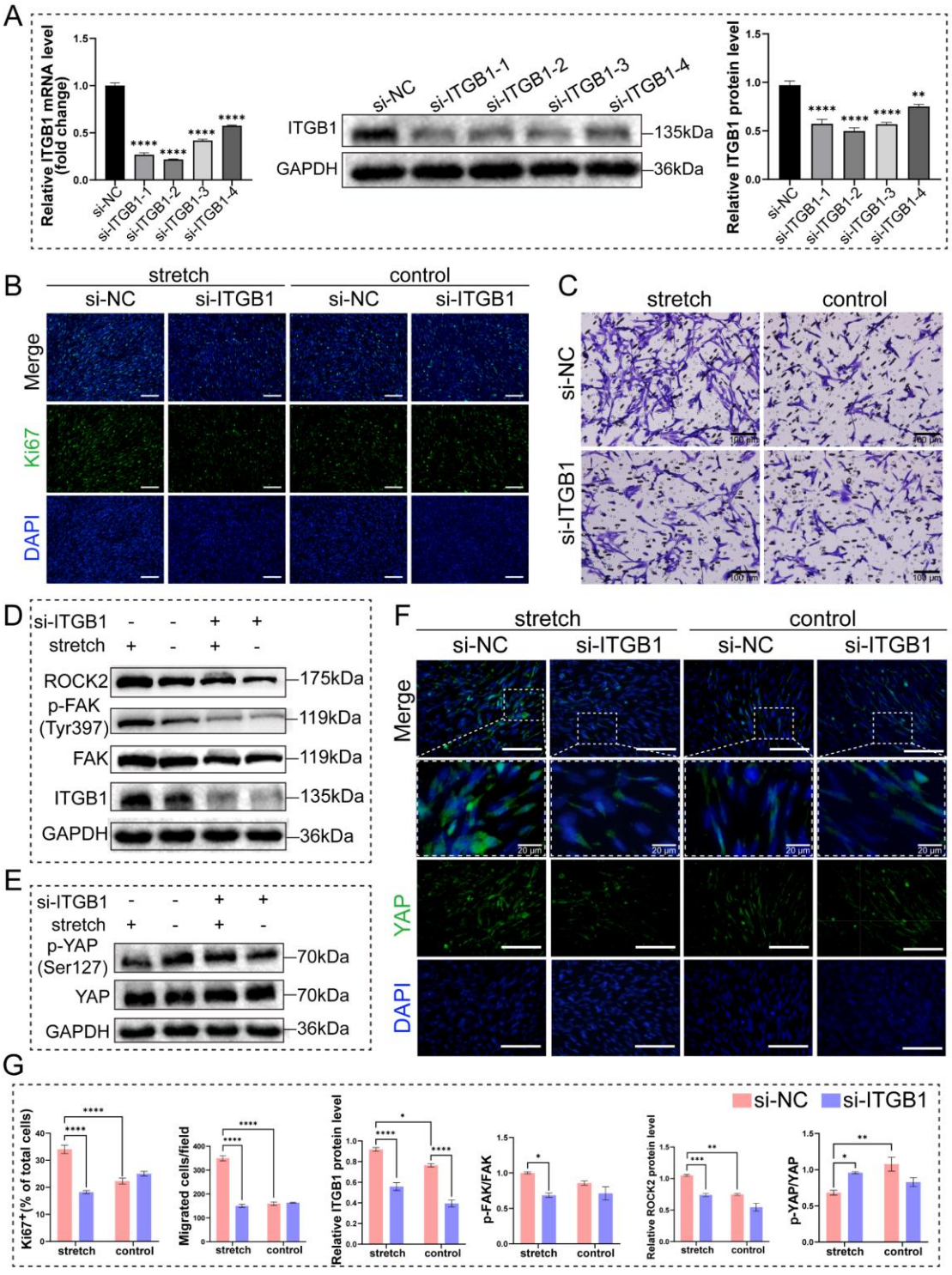

A
Relative ITGB1 mRNA level (fold change)
si-NC
si-ITGB1-1
si-ITGB1-2
si-ITGB1-3
si-ITGB1-4
ITGB1
GAPDH
135kDa
36kDa
Relative ITGB1 protein level
B
stretch
control
si-NC
si-ITGB1
Merge
Ki67
DAPI
C
stretch
control
si-NC
si-ITGB1
D
si-ITGB1
stretch
ROCK2
p-FAK (Tyr397)
FAK
ITGB1
GAPDH
175kDa
119kDa
119kDa
135kDa
36kDa
E
si-ITGB1
stretch
p-YAP (Ser127)
YAP
GAPDH
70kDa
70kDa
36kDa
F
stretch
control
si-NC
si-ITGB1
Merge
YAP
DAPI
G
si-NC
si-ITGB1
Ki67+ (% of total cells)
Migrated cells/field
Relative ITGB1 protein level
p-FAK/FAK
Relative ROCK2 protein level
p-YAP/YAP
stretch
control

Figure 8

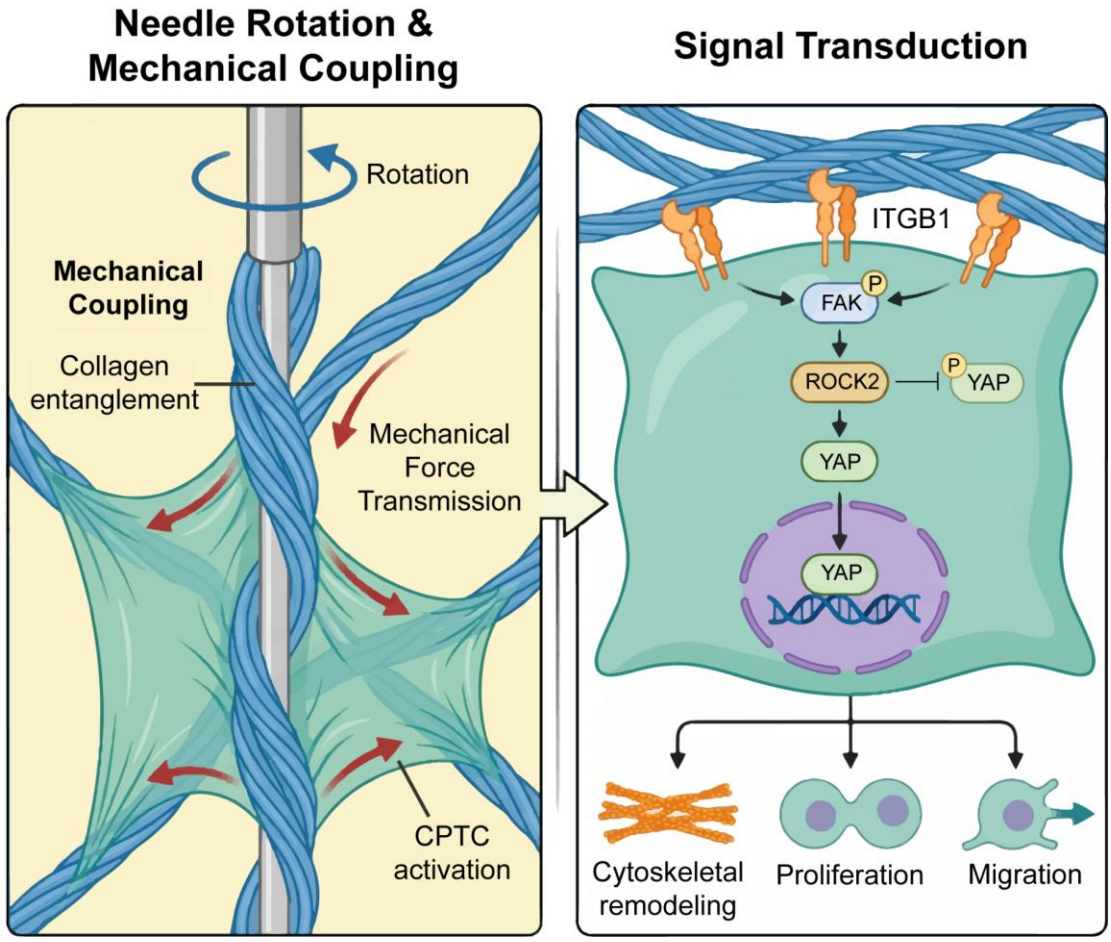

Needle Rotation &
Mechanical Coupling
Signal Transduction
Rotation
Mechanical
Coupling
Collagen
entanglement
Mechanical
Force
Transmission
CPTC
activation
ITGB1
FAK
P
ROCK2
P
YAP
YAP
YAP
Cytoskeletal
remodeling
Proliferation
Migration

Figure S1

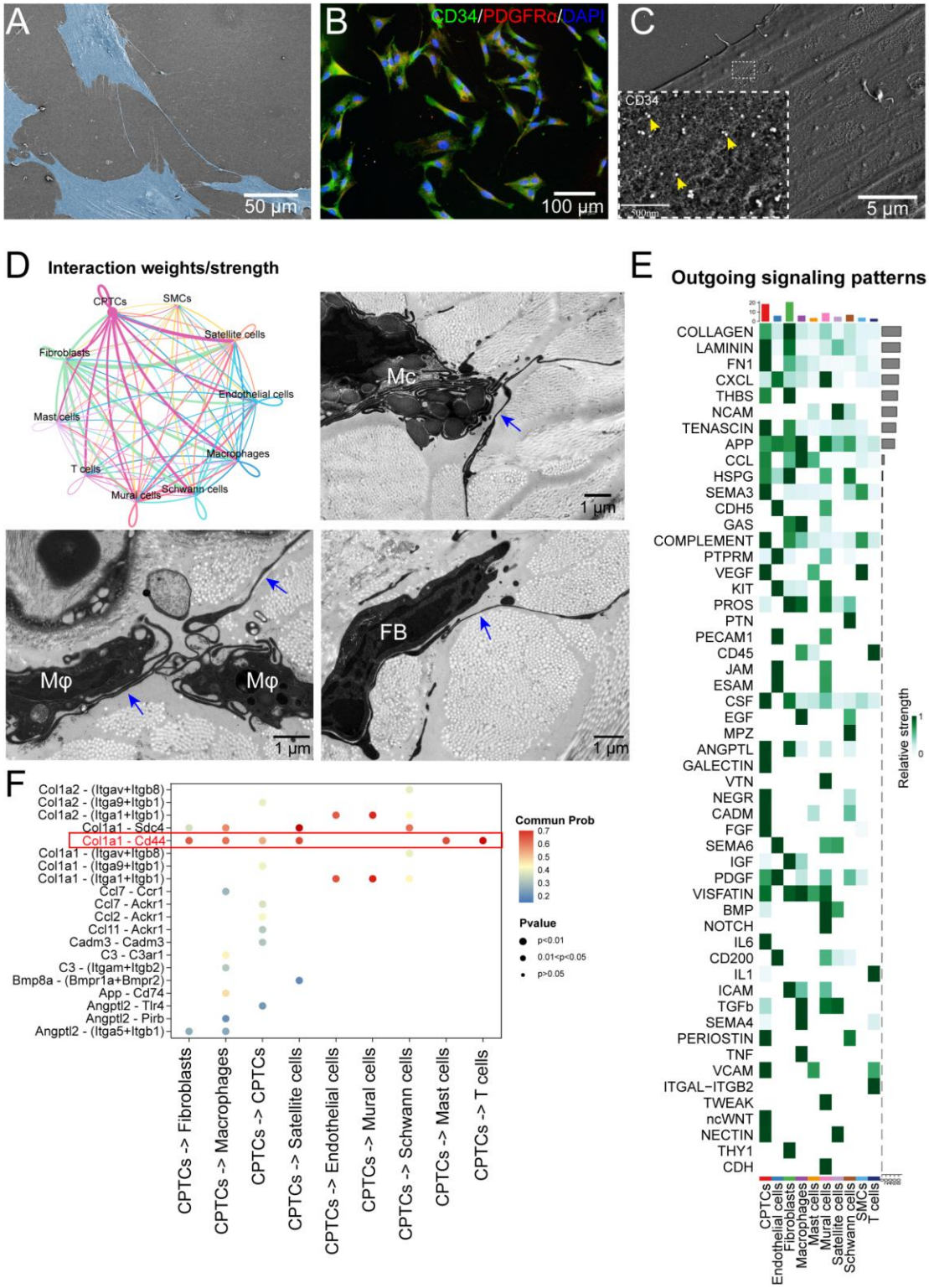

A
50 μm
B
CD34/PDGFRα/DAPI
100 μm
C
CD34
5 μm
D
Interaction weights/strength
CPTCs
SMCs
Satellite cells
Fibroblasts
Endothelial cells
Mast cells
Macrophages
T cells
Mural cells
Schwann cells
Mc
1 μm
Mφ
Mφ
1 μm
FB
1 μm
E
Outgoing signaling patterns
COLLAGEN
LAMININ
FN1
CXCL
THBS
NCAM
TENASCIN
APP
CCL
HSPG
SEMA3
CDH5
GAS
COMPLEMENT
PTPRM
VEGF
KIT
PROS
PTN
PECAM1
CD45
JAM
ESAM
CSF
EGF
MPZ
ANGPTL
GALECTIN
VTN
NEGR
CADM
FGF
SEMA6
IGF
PDGF
VISFATIN
BMP
NOTCH
IL6
CD200
IL1
ICAM
TGFb
SEMA4
PERIOSTIN
TNF
VCAM
ITGAL−ITGB2
TWEAK
ncWNT
NECTIN
THY1
CDH
CPTCs
Endothelial cells
Fibroblasts
Macrophages
Mast cells
Mural cells
Satellite cells
Schwann cells
SMCs
T cells
Relative strength
F
Col1a2 - (Itgav+Itgb8)
Col1a2 - (Itga9+Itgb1)
Col1a2 - (Itga1+Itgb1)
Col1a1 - Sdc4
Col1a1 - Cd44
Col1a1 - (Itgav+Itgb8)
Col1a1 - (Itga9+Itgb1)
Col1a1 - (Itga1+Itgb1)
Ccl7 - Ccr1
Ccl7 - Ackr1
Ccl2 - Ackr1
Ccl11 - Ackr1
Cadm3 - Cadm3
C3 - C3ar1
C3 - (Itgam+Itgb2)
Bmp8a - (Bmpr1a+Bmpr2)
App - Cd74
Angptl2 - Tlr4
Angptl2 - Pirb
Angptl2 - (Itga5+Itgb1)
CPTCs -> Fibroblasts
CPTCs -> Macrophages
CPTCs -> CPTCs
CPTCs -> Satellite cells
CPTCs -> Endothelial cells
CPTCs -> Mural cells
CPTCs -> Schwann cells
CPTCs -> Mast cells
CPTCs -> T cells
Commun Prob
Pvalue
p<0.01
0.01<p<0.05
p>0.05

Figure S2

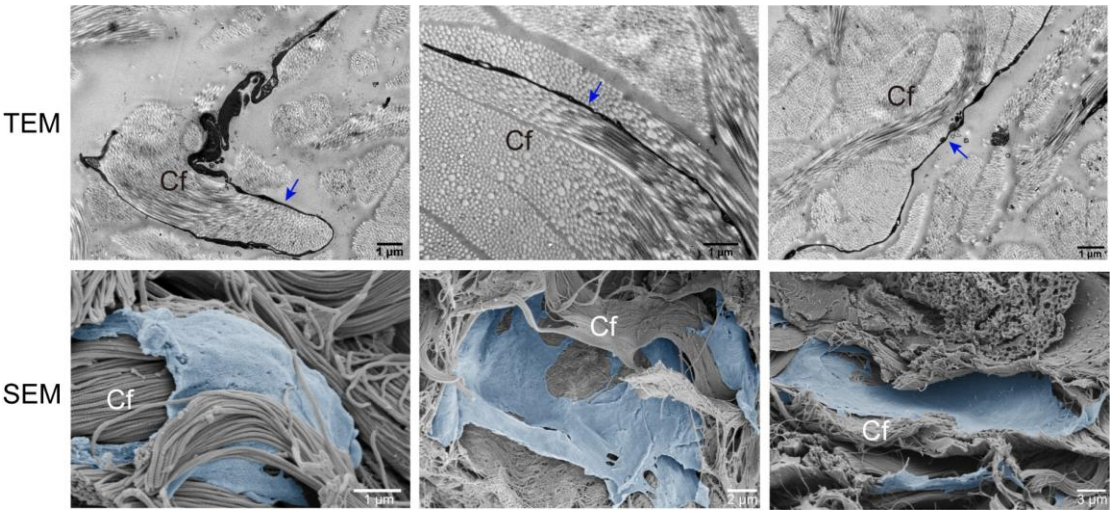


Figure S3

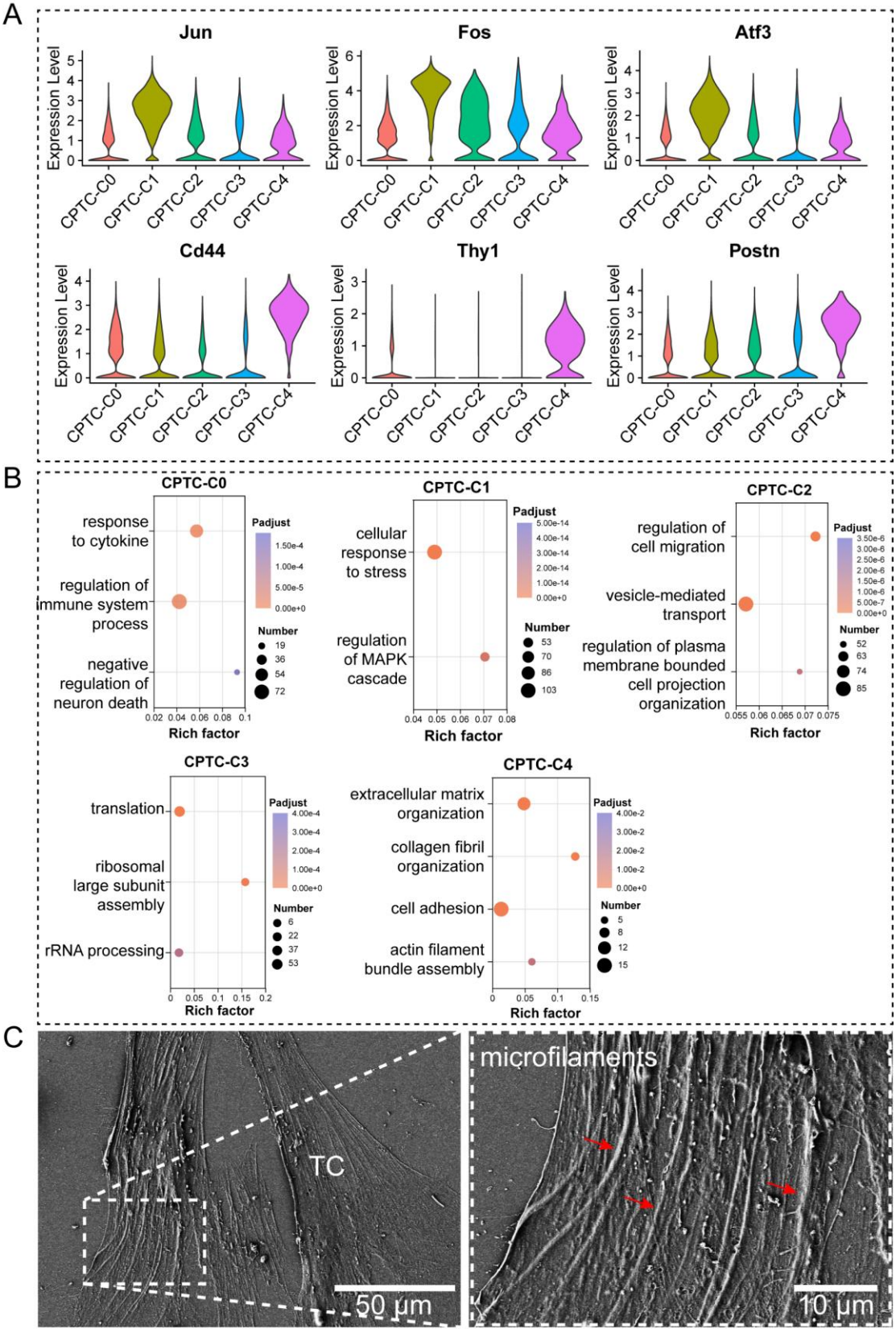
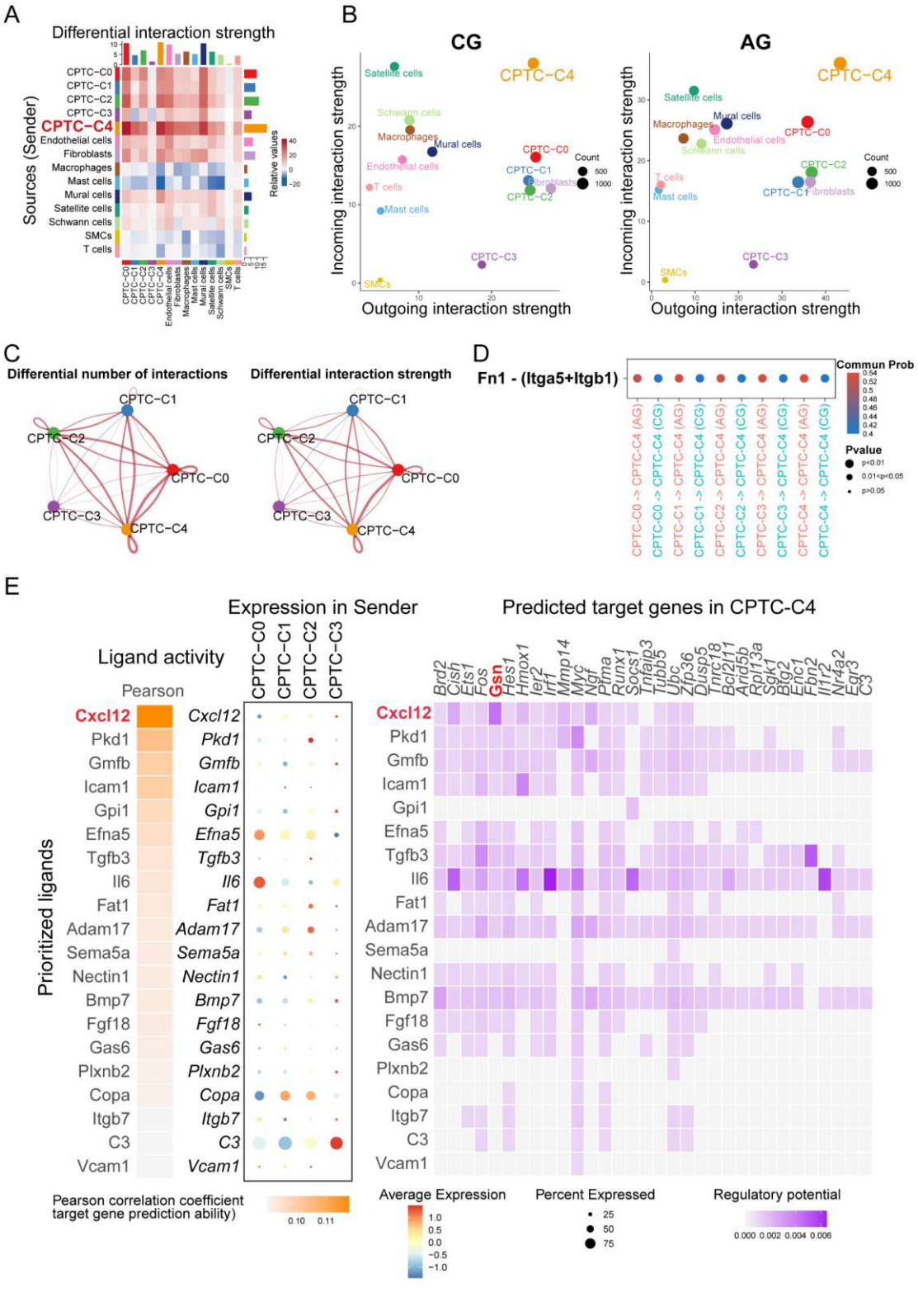
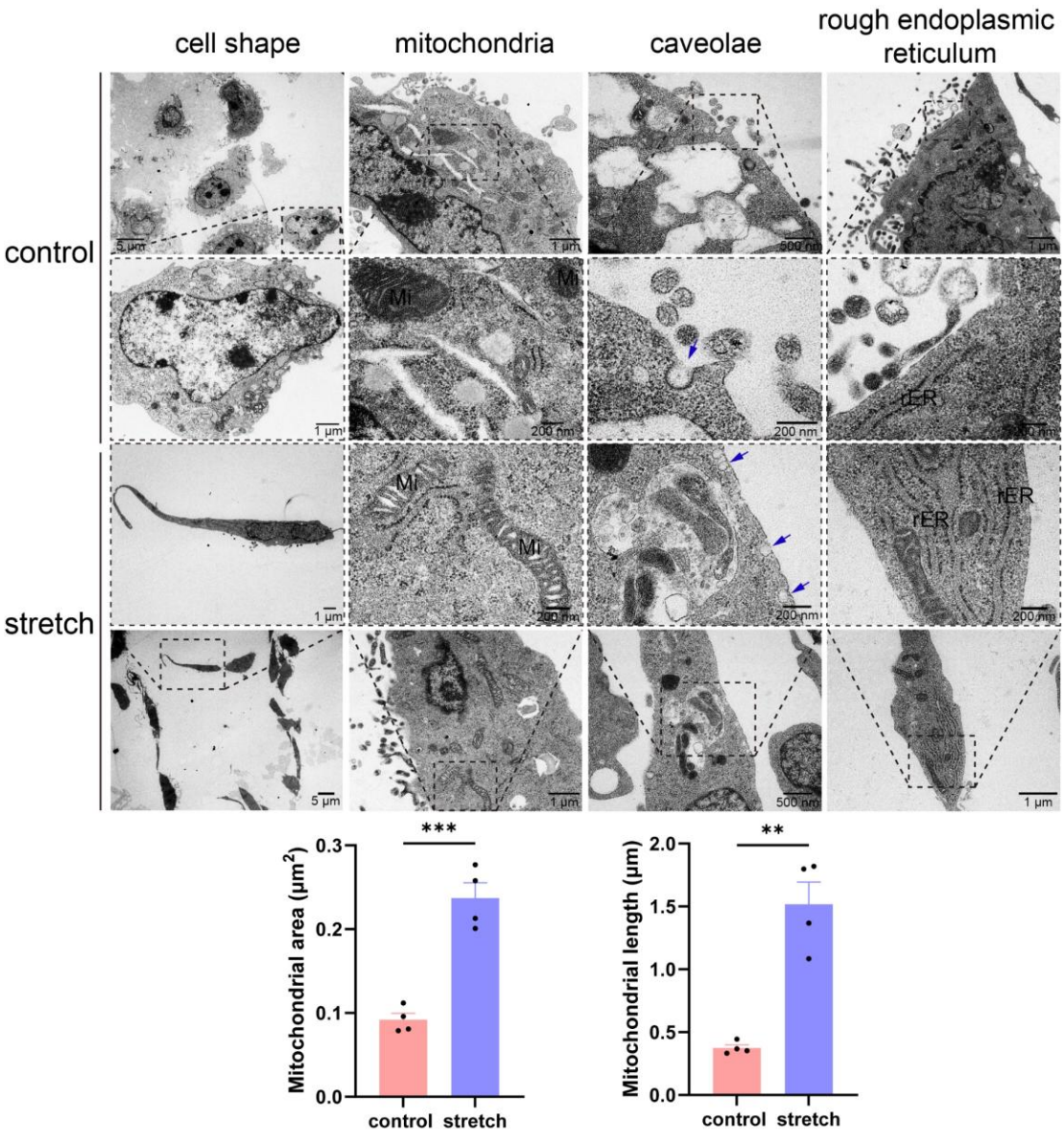

A
Jun
Fos
Atf3
Cd44
Thy1
Postn
Expression Level
CPTC-C0
CPTC-C1
CPTC-C2
CPTC-C3
CPTC-C4
B
CPTC-C0
response to cytokine
regulation of immune system process
negative regulation of neuron death
CPTC-C1
cellular response to stress
regulation of MAPK cascade
CPTC-C2
regulation of cell migration
vesicle-mediated transport
regulation of plasma membrane bounded cell projection organization
CPTC-C3
translation
ribosomal large subunit assembly
rRNA processing
CPTC-C4
extracellular matrix organization
collagen fibril organization
cell adhesion
actin filament bundle assembly
Rich factor
Padjust
Number
C
TC
50 μm
microfilaments
10 μm

Figure S4


A
Differential interaction strength
Sources (Sender)
CPTC-C0
CPTC-C1
CPTC-C2
CPTC-C3
CPTC-C4
Endothelial cells
Fibroblasts
Macrophages
Mast cells
Mural cells
Satellite cells
Schwann cells
SMCs
T cells
Relative values
B
CG
AG
Incoming interaction strength
Outgoing interaction strength
Count
C
Differential number of interactions
Differential interaction strength
D
Fn1 - (Itga5+Itgb1)
Commun Prob
Pvalue
E
Expression in Sender
Predicted target genes in CPTC-C4
Ligand activity
Pearson
Prioritized ligands
Cxcl12
Pkd1
Gmfb
Icam1
Gpi1
Efna5
Tgfb3
Il6
Fat1
Adam17
Sema5a
Nectin1
Bmp7
Fgf18
Gas6
Plxnb2
Copa
Itgb7
C3
Vcam1
Pearson correlation coefficient target gene prediction ability)
Average Expression
Percent Expressed
Regulatory potential

729 **Figure S5**



730
731

References

1. Wang J, Lu S, Yang F, Guo Y, Chen Z, Yu N, et al. The role of macrophage polarization and associated mechanisms in regulating the anti-inflammatory action of acupuncture: a literature review and perspectives. Chin Med 2021; 16 (1): 56. doi: 10.1186/s13020-021-00466-7.
2. Gamus D, Shoenfeld Y. Acupuncture therapy in autoimmune diseases: A narrative review. Autoimmun Rev 2025; 24 (2): 103709. doi: 10.1016/j.autrev.2024.103709.
3. Wen J, Chen X, Yang Y, Liu J, Li E, Liu J, et al. Acupuncture Medical Therapy and its Underlying Mechanisms: A Systematic Review. Am J Chin Med 2021; 49 (1): 1-23. doi: 10.1142/S0192415X21500014.
4. Lu Z, Wang M, Chen W, Jin M, Zhu L, Wang T, et al. High numerical aperture confocal volumetric mesoscope reveals mesoscale subcellular dynamics in vivo. Nat Biotechnol 2026; doi: 10.1038/s41587-026-03231-z.
5. Liu S, Wang Z, Su Y, Qi L, Yang W, Fu M, et al. A neuroanatomical basis for electroacupuncture to drive the vagal-adrenal axis. Nature 2021; 598 (7882): 641-645. doi: 10.1038/s41586-021-04001-4.
6. Yunshan L, Chengli X, Peiming Z, Haocheng Q, Xudong L, Liming L. Integrative research on the mechanisms of acupuncture mechanics and interdisciplinary innovation. Biomed Eng Online 2025; 24 (1): 30. doi: 10.1186/s12938-025-01357-w.
7. Han S. The role of mechanoreceptors in acupuncture. Medicine in Novel Technology and Devices 2023; 17 100207. doi: https://doi.org/10.1016/j.medntd.2023.100207.
8. Langevin HM, Churchill DL, Cipolla MJ. Mechanical signaling through connective tissue: a mechanism for the therapeutic effect of acupuncture. FASEB journal : official publication of the Federation of American Societies for Experimental Biology 2001; 15 (12): 2275-2282. doi: 10.1096/fj.01-0015hyp.
9. Langevin HM, Churchill DL, Wu J, Badger GJ, Yandow JA, Fox JR, et al. Evidence of connective tissue involvement in acupuncture. FASEB journal : official publication of the Federation of American Societies for Experimental Biology 2002; 16 (8): 872-874. doi: 10.1096/fj.01-0925fje.
10. Bai X, Mei L, Shi Y, Huang H, Guo Y, Liang C, et al. The Cellular Mechanism of Acupuncture for Ulcerative Colitis based on the Communication of Telocytes. Microscopy and microanalysis : the official journal of Microscopy Society of America, Microbeam Analysis Society, Microscopical Society of Canada 2023; 29 (3): 1190-1204. doi: 10.1093/micmic/ozad028.
11. Dai M, Mei L, Lu L, Zhu Q, Bai X, Yang T, et al. Discovery of the Animal Acupoint "Telocyte-Entanglement Complex" and Its Ultrastructural Characteristics. Scientia Agricultura Sinica 2026; 59 (11): 2526-2536.
12. Popescu LM, Faussone-Pellegrini M-S. TELOCYTES - a case of serendipity: the winding way from Interstitial Cells of Cajal (ICC), via Interstitial Cajal-Like Cells (ICLC) to TELOCYTES. Journal of Cellular and Molecular Medicine 2010; 14 (4): 729-740. doi: 10.1111/j.1582-4934.2010.01059.x.
13. Huang H, Shi Y, Shen B, Zhang Z, Yue J, Mei L, et al. Application of single-cell deep learning in elucidating the mapping relationship between visceral and body surface inflammatory patterns. Comput Struct Biotechnol J 2025; 27 4183-4200. doi:

776 10.1016/j.csbj.2025.09.040.
777 14. Zhang Z, Huang H, Yue J, Zhu X, Shi Y, Shen B, et al. Ptgs2+ CPTC Function as a "Force-
778 Immune Axis" by Responding to Acupuncture and Mediating M2 Macrophage Activation
779 for Anti-Inflammatory Effects. FASEB journal : official publication of the Federation of
780 American Societies for Experimental Biology 2025; 39 (19): e71048. doi:
781 10.1096/fj.202501175RR.
782 15. Huang H, Zhang Z, Shen B, Yue J, Mei L, Zhu X, et al. CPTCs Drive Somatic-Visceral
783 Communication via the Wnt Axis in Somatic Mechanotherapy: A Single-Cell Deep
784 Learning Study. FASEB journal : official publication of the Federation of American Societies
785 for Experimental Biology 2026; 40 (15): e72176. doi: 10.1096/fj.202600755RRR.
786 16. Wang Y, Zhang Q, Wu S, Hu K, Bu S, Song Y, et al. Electroacupuncture-based vagal
787 stimulation attenuates epileptic seizures through a body-brain circuit. Proc Natl Acad Sci
788 U S A 2026; 123 (12): e2517600123. doi: 10.1073/pnas.2517600123.
789 17. Wang X, Shi SH, Yao HJ, Jing QK, Mo YP, Lv W, et al. Electroacupuncture at Dazhui (GV14)
790 and Mingmen (GV4) protects against spinal cord injury: the role of the Wnt/beta-catenin
791 signaling pathway. Neural Regen Res 2016; 11 (12): 2004-2011. doi: 10.4103/1673-
792 5374.197145.
793 18. Kimura M, Tohya K, Kuroiwa K, Oda H, Gorawski EC, Hua ZX, et al. Electron microscopical
794 and immunohistochemical studies on the induction of "Qi" employing needling
795 manipulation. Am J Chin Med 1992; 20 (1): 25-35. doi: 10.1142/S0192415X92000047.
796 19. Li Y, Zhang X, Gao J, Xiao H, Xu M. Increased telocytes involved in the proliferation of
797 vascular smooth muscle cells in rat carotid artery balloon injury. Sci China Life Sci 2016;
798 59 (7): 678-685. doi: 10.1007/s11427-016-5075-9.
799 20. Sheng W, Wang R, Xue X, Zhao P, Zhang J, Tseng Y. From mechanosensing to immune
800 regulation: mechanisms of acupuncture signal initiation and amplification mediated by
801 macrophages. Front Immunol 2026; 17 1744045. doi: 10.3389/fimmu.2026.1744045.
802 21. Tu S, Li Y, Li J, Ma N, Yao K, Chen Z, et al. Mechanical stretch-mediated fibroblast
803 activation: The pivotal role of Piezo1 channels. Biochim Biophys Acta Mol Cell Res 2025;
804 1872 (7): 120008. doi: 10.1016/j.bbamcr.2025.120008.
805 22. Hilfiker-Kleiner D, Kaminski K, Kaminska A, Fuchs M, Klein G, Podewski E, et al. Regulation
806 of proangiogenic factor CCN1 in cardiac muscle: impact of ischemia, pressure overload,
807 and neurohumoral activation. Circulation 2004; 109 (18): 2227-2233. doi:
808 10.1161/01.CIR.0000127952.90508.9D.
809 23. Yoshigi M, Hoffman LM, Jensen CC, Yost HJ, Beckerle MC. Mechanical force mobilizes
810 zyxin from focal adhesions to actin filaments and regulates cytoskeletal reinforcement.
811 The Journal of cell biology 2005; 171 (2): 209-215. doi: 10.1083/jcb.200505018.
812 24. Sanches BDA, Teófilo FBS, Brunet MY, Villapun VM, Man K, Rocha LC, et al. Telocytes:
813 current methods of research, challenges and future perspectives. Cell Tissue Res 2024;
814 396 (2): 141-155. doi: 10.1007/s00441-024-03888-5.
815 25. Dupont S, Morsut L, Aragona M, Enzo E, Giulitti S, Cordenonsi M, et al. Role of YAP/TAZ
816 in mechanotransduction. Nature 2011; 474 (7350): 179-183. doi: 10.1038/nature10137.
817 26. Xiao B. Mechanisms of mechanotransduction and physiological roles of PIEZO channels.
818 Nat Rev Mol Cell Biol 2024; 25 (11): 886-903. doi: 10.1038/s41580-024-00773-5.
819 27. Cox CD, Poole K, Martinac B. Re-evaluating TRP channel mechanosensitivity. Trends

Biochem Sci 2024; 49 (8): 693-702. doi: 10.1016/j.tibs.2024.05.004.
28. Kechagia JZ, Ivaska J, Roca-Cusachs P. Integrins as biomechanical sensors of the microenvironment. Nat Rev Mol Cell Biol 2019; 20 (8): 457-473. doi: 10.1038/s41580-019-0134-2.
29. Weinbaum S, Tarbell JM, Damiano ER. The structure and function of the endothelial glycocalyx layer. Annu Rev Biomed Eng 2007; 9 121-167. doi: 10.1146/annurev.bioeng.9.060906.151959.
30. Sun Z, Guo SS, Fassler R. Integrin-mediated mechanotransduction. The Journal of cell biology 2016; 215 (4): 445-456. doi: 10.1083/jcb.201609037.
31. Schwartz MA. Integrins and extracellular matrix in mechanotransduction. Cold Spring Harbor perspectives in biology 2010; 2 (12): a005066. doi: 10.1101/cshperspect.a005066.
32. Zhang JJ, Li X, Tian Y, Zou JK, Gan D, Deng DK, et al. Harnessing Mechanical Stress with Viscoelastic Biomaterials for Periodontal Ligament Regeneration. Adv Sci (Weinh) 2024; 11 (18): e2309562. doi: 10.1002/advs.202309562.
33. Wen H, Blume PA, Sumpio BE. Role of integrins and focal adhesion kinase in the orientation of dermal fibroblasts exposed to cyclic strain. Int Wound J 2009; 6 (2): 149-158. doi: 10.1111/j.1742-481X.2009.00591.x.
34. Langevin HM, Bouffard NA, Badger GJ, Churchill DL, Howe AK. Subcutaneous tissue fibroblast cytoskeletal remodeling induced by acupuncture: evidence for a mechanotransduction-based mechanism. J Cell Physiol 2006; 207 (3): 767-774. doi: 10.1002/jcp.20623.
35. Yang L, Jiang P, Stein JB, Hou Y, Zhou C, Kang H, et al. Mechanobiological Dynamics-Inspired Mechanomodulatory Biomaterials. Adv Sci (Weinh) 2026; 13 (4): e16992. doi: 10.1002/advs.202416992.
36. Del Pozo MA, Lolo FN, Echarri A. Caveolae: Mechanosensing and mechanotransduction devices linking membrane trafficking to mechanoadaptation. Curr Opin Cell Biol 2021; 68 113-123. doi: 10.1016/j.ceb.2020.10.008.
37. Fernandez-Fernandez MR, Valpuesta JM. Hsp70 chaperone: a master player in protein homeostasis. F1000Res 2018; 7 doi: 10.12688/f1000research.15528.1.
38. Halder G, Dupont S, Piccolo S. Transduction of mechanical and cytoskeletal cues by YAP and TAZ. Nat Rev Mol Cell Biol 2012; 13 (9): 591-600. doi: 10.1038/nrm3416.
39. Zhao B, Ye X, Yu J, Li L, Li W, Li S, et al. TEAD mediates YAP-dependent gene induction and growth control. Genes Dev 2008; 22 (14): 1962-1971. doi: 10.1101/gad.1664408.
40. Codelia VA, Sun G, Irvine KD. Regulation of YAP by mechanical strain through Jnk and Hippo signaling. Current biology : CB 2014; 24 (17): 2012-2017. doi: 10.1016/j.cub.2014.07.034.
41. Nava MM, Miroshnikova YA, Biggs LC, Whitefield DB, Metge F, Boucas J, et al. Heterochromatin-Driven Nuclear Softening Protects the Genome against Mechanical Stress-Induced Damage. Cell 2020; 181 (4): 800-817 e822. doi: 10.1016/j.cell.2020.03.052.
42. Koushki N, Ghagre A, Srivastava LK, Molter C, Ehrlicher AJ. Nuclear compression regulates YAP spatiotemporal fluctuations in living cells. Proc Natl Acad Sci U S A 2023; 120 (28): e2301285120. doi: 10.1073/pnas.2301285120.
43. Tu SW, Kawanokuchi J, Takagi K, Liu YY, Li JY, Deng KY, et al. Fibroblasts as key effectors of acupuncture in treatment of rheumatoid arthritis. Front Immunol 2026; 17 1715313.

doi: 10.3389/fimmu.2026.1715313.

44. Yao W, Yang H, Yin N, Ding G. Mast cell-nerve cell interaction at acupoint: modeling mechanotransduction pathway induced by acupuncture. Int J Biol Sci 2014; 10 (5): 511-519. doi: 10.7150/ijbs.8631.

Figure legends

Figure 1. Morphological and transcriptomic characterization of CPTCs in the mouse dorsal midline Sf. (A) Schematic of tissue sampling from the dorsal midline of normal mice for IF, TEM, SEM, and scRNA-seq. (B) Representative H&E-stained section showing the histological architecture of the dorsal midline region, including the Ep, De, Pc, and Sf. The boxed region is enlarged in (b). (C) Representative IF image showing $CD34^+$ (green)/$PDGFR\alpha^+$ (red) TCs within the Sf. Nuclei are counterstained with DAPI (blue). (D) TEM image showing a CPTC with long, slender telopodes (red arrows). (E) Representative SEM image showing the broad, flattened membranous morphology of a CPTC, highlighted by blue pseudocolouring and a white asterisk. (F) UMAP visualization of the cellular landscape from dorsal midline Sf in CG, identifying ten annotated cell types: CPTCs, fibroblasts, endothelial cells, macrophages, satellite cells, mast cells, T cells, mural cells, SMCs (skeletal muscle cells), and Schwann cells. (G) Dot plot showing representative marker genes used to annotate the cell populations. (H) Box plots showing the proportions of the identified cell populations, calculated separately for each independently sequenced CG sample. (I) GSVA heatmap of "cellular response to mechanical stimulus" and "response to mechanical stimulus" across cell populations. (J) Heatmap showing the expression of genes associated with responses to mechanical stimuli across cell populations. Each column represents an individual cell, and the top annotation bar indicates cell identity. (K) GO GSEA showing positive enrichment of "extracellular matrix assembly" in CPTCs relative to other cell types. (L) Representative TEM image showing focal adhesion structures (blue arrows) between a CPTC and the ECM. Ep: epidermis; De: dermis; Sf: subcutaneous fascia; Pc: panniculus carnosus. Scale bars: 500 μm (B); 50 μm (b, C); 5 μm (D, E); 500 nm (L).

Figure 2. Structural association of CPTCs with collagen fibers in needle-adherent tissue. (A) Schematic of needle-adherent tissue collection following manual acupuncture. Some specimens were fixed together with the needles for SEM, whereas others were detached for morphological analysis. (B) Representative SEM image showing tissue wrapped around the needle shaft. (C) SEM image showing a dense network of interwoven collagen fibers on the tissue surface. (D) SEM image showing broad, flattened membranous CPTC extensions (pseudocoloured blue) among collagen bundles. The boxed region is enlarged in (d). (E) SEM image showing the hollow tubular architecture of the tissue after removal from the needle. (F) Masson's trichrome

staining showing collagen fibers (blue) and Pc (red) within the tubular tissue wall. (G) TEM image showing a slender CPTC process (pseudocoloured blue; black arrow) interspersed among collagen fibers. (H) Representative IF images showing $CD34^+$ (green)/$PDGFR\alpha^+$ (red) TCs within the tubular tissue wall. Nuclei are counterstained with DAPI (blue). The boxed region in the merged image is enlarged on the right, with white arrows indicating CPTCs. Cf: collagen fibers; Pc: panniculus carnosus. Scale bars: 100 μm (B, E); 2 μm (C, D); 500 nm (d); 50 μm (F, H overview); 1 μm (G); 20 μm (H enlargement).

Figure 3. Acupuncture increased CPTC density and enhanced transcriptional signatures associated with proliferation and mechanical responses. (A) Schematic of the experimental workflow. Mice received manual acupuncture at GV14 and GV4 for 15 min daily for 7 days, followed by dorsal midline tissue collection for scRNA-seq and morphological analyses. (B) t-SNE plots showing the distribution of cell populations in CG and AG. (C) Relative proportions of the identified cell populations in each group. (D) Proportions of CPTCs assigned to the G1, S, and G2/M phases in individual samples. (E) KEGG GSEA showing enrichment of DNA replication in AG CPTCs relative to CG. (F) Representative IF images showing $CD34^+$ (green)/$PDGFR\alpha^+$ (red) TCs in Sf. White arrows indicate CPTCs, and nuclei are counterstained with DAPI (blue). (G) Representative TEM images showing CPTCs and their slender processes (red arrows) among collagen fibers. (H) CellChat heatmap showing differences in predicted interaction strength between AG and CG. Rows and columns represent sender and receiver populations, respectively; red and blue indicate increased and decreased interaction strength in AG relative to CG. (I) Chord diagram linking selected genes upregulated in AG CPTCs to enriched GO terms associated with mechanical responses, actin filament bundle assembly, focal adhesion, and extracellular matrix assembly. (J) Quantification of CPTC density in Sf, expressed as the number of CPTCs per mm^2 (n = 10 mice per group). (K) KEGG GSEA of selected enriched pathways in CPTCs comparing AG with CG. ****$P < 0.0001$. Scale bars: 20 μm (F); 5 μm (G).

Figure 4. CPTC subpopulations exhibited transcriptional heterogeneity and distinct responses to acupuncture. (A) UMAP visualization of five CPTC subclusters identified in CG. (B) Dot plot showing representative marker genes across CG CPTC subclusters. (C) Relative proportions of CPTC subclusters in CG and AG. (D) Volcano plot showing differential gene expression in CPTC-C1 between AG and CG, with selected stress-associated genes labeled. (E) Slingshot-inferred trajectory of AG CPTCs,

with CPTC-C2 designated as the root. (F) RNA velocity vector field of AG CPTCs projected onto the UMAP embedding. Arrows indicate the inferred direction of transcriptional state transitions. (G) GSVA heatmap of "response to mechanical stimulus" and "cellular response to mechanical stimulus" across CG CPTC subclusters. (H) Violin plots showing the expression of *Piezo1*, *Trpv4*, *Itga5*, and *Itgb1* across CG CPTC subclusters. (I) Volcano plot showing differential gene expression in CPTC-C4 between AG and CG, with selected adhesion- and cytoskeleton-associated genes labeled. (J) Chord diagram linking selected genes upregulated in AG CPTC-C4 to enriched KEGG pathways, including ECM–receptor interaction, regulation of actin cytoskeleton, and focal adhesion. (K) GSEA of selected KEGG pathways in CPTC-C4 from the AG-versus-CG comparison.

Figure 5. Cyclic stretching promoted CPTC proliferation, cytoskeletal remodeling, and migration. (A) Schematic of the experimental workflow. CPTCs were subjected to cyclic stretching at 15% strain and 0.5 Hz or maintained under static conditions. (B) Representative images showing CPTC morphology after 1, 3, and 6 h. Blue arrows indicate the stretching direction. (C) WB images showing CD34 and PDGFRα expression at the indicated time points, with GAPDH as the loading control. (D) Representative flow cytometry histograms showing cell-cycle distributions in control and stretched CPTCs at 6 h. (E) Quantification of CD34 and PDGFRα protein levels normalized to GAPDH (n = 3) and cell-cycle phase distribution (n = 3). (F) Representative IF images showing Ki67 (green) and DAPI-stained nuclei (blue) after 6 h of stretching. (G) Representative images showing phalloidin-stained F-actin and DAPI-stained nuclei after 6 h of stretching. (H) Scratch wound images acquired at 0, 12, and 24 h after scratching (following 6 h of stretching). White lines delineate the wound edges. (I) Representative images of cells that migrated through Transwell membranes at 24 h. (J) Quantification of the $Ki67^+$ cell percentage (n = 9), single-cell spreading area (n = 10), scratch wound closure at 12 and 24 h (n = 3), and migrated cells per field in the Transwell assay (n = 6). *P < 0.05, **P < 0.01, ***P < 0.001, and ****P < 0.0001. Scale bars: 100 μm (B, F, I); 50 μm (G); 200 μm (H).

Figure 6. Cyclic stretching altered adhesion-associated proteins and promoted YAP nuclear translocation in CPTCs. (A) Volcano plot showing differential protein abundance in the two groups of CPTCs. (B–D) Subcellular localization, GO functional classification, and KEGG enrichment analysis of all 230 DEPs. (E) Heatmap showing the relative abundance of four upregulated heat shock proteins. (F) GSEA plots showing

enrichment of heat shock protein binding and ATP-dependent protein folding chaperone functions in stretched CPTCs. (G) Representative SEM images showing cell morphology, focal adhesions, and adherens junctions after 6 h of stretching. Blue dashed lines outline cells, purple dashed lines mark focal adhesion structures, and red arrows indicate adherens junctions. (H) Representative WB images and quantification of ITGA5, ITGB1, ROCK2, p-FAK (Tyr397), FAK, p-YAP (Ser127), YAP, and E-cadherin at 1, 3, and 6 h (n = 3). GAPDH served as the loading control; p-FAK/FAK and p-YAP/YAP ratios are shown. The rightmost plot shows the percentage of nuclear YAP-positive cells corresponding to (I) (n = 9 per group). (I) Representative IF images showing YAP (green) and DAPI-stained nuclei (blue) after 6 h of stretching. (J) TEM image showing a marked reduction in perinuclear heterochromatin in stretched CPTCs. (K) STRING PPI network showing functional associations among the four selected candidate proteins ITGB1, FAK, ROCK2, and YAP, labeled with their corresponding gene symbols. *P < 0.05, **P < 0.01, ***P < 0.001, and ****P < 0.0001. Scale bars: 100 μm and 20 μm for the overview and enlarged images in (I), respectively; other scale bars are indicated in (G, J).

Figure 7. ITGB1 knockdown attenuated stretch-induced proliferation, migration, and YAP nuclear translocation in CPTCs. (A) Screening of four siRNAs targeting ITGB1 by qPCR and WB 48 h after transfection (n = 3 for each assay). si-ITGB1-2 was selected for subsequent experiments. (B) Representative IF images showing Ki67 (green) and DAPI-stained nuclei (blue) in CPTCs from four groups: si-NC, si-ITGB1, si-NC + stretch, and si-ITGB1 + stretch. Cyclic stretching was applied at 15% strain and 0.5 Hz for 6 h. (C) Representative Transwell images showing migrated cells at 24 h. (D, E) WB images showing ITGB1, ROCK2, p-FAK (Tyr397), FAK, p-YAP (Ser127), and YAP in the four experimental groups. GAPDH served as the loading control. (F) Representative IF images showing YAP (green) and DAPI-stained nuclei (blue). Boxed regions in the merged images are shown at higher magnification below. (G) Quantification of the $Ki67^+$ cell percentage and migrated cells per field (n = 6 each), together with WB quantification of ITGB1, ROCK2, p-FAK/FAK, and p-YAP/YAP (n = 3 each). *P < 0.05, **P < 0.01, ***P < 0.001, and ****P < 0.0001. Scale bars: 100 μm (B, C, and overview images in F); 20 μm (enlarged images in F).

Figure 8. Schematic representation of CPTC-mediated ITGB1-dependent mechanotransduction mechanism following acupuncture.

Figure S1. CPTCs exhibited membranous morphology and extensive predicted communication with other fascial cells. (A) SEM image showing primary cultured CPTCs isolated from the dorsal midline Sf of normal mice. Blue pseudocoloring highlights the flattened cell bodies and extensions. (B) Representative IF image showing CD34 (green), PDGFRα (red), and DAPI-stained nuclei (blue) in cultured CPTCs. (C) Representative immunogold SEM image showing CD34 labeling on the cell surface. The boxed region is enlarged in the inset, with yellow arrowheads indicating gold particles. (D) CellChat network showing predicted interaction strengths among fascial cell populations in CG, accompanied by representative TEM images showing CPTC slender processes (blue arrows) closely associated with Mc mast cells, Mφ macrophages, and Fb fibroblasts. (E) Heatmap showing outgoing signaling patterns across cell populations in CG. (F) Bubble plot showing selected predicted ligand–receptor interactions from CPTCs to the indicated receiver populations in CG. The red box highlights predicted *Col1a1–Cd44* interactions. Scale bars: 50 μm (A); 100 μm (B); 5 μm (C), with 500 nm in the inset; 1 μm (D, TEM images).

Figure S2. CPTCs exhibited three spatial relationships with collagen bundles in Sf. Representative TEM (upper row) and SEM (lower row) images of the dorsal midline Sf from normal mice. TEM images showed slender CPTC processes (blue arrows) wrapping around collagen bundles, extending between adjacent bundles, or closely adhering to one side. SEM images revealed corresponding spatial arrangements between broad, flattened CPTC extensions (pseudocoloured blue) and collagen bundles, consistent with the TEM observations.

Figure S3. CPTC subpopulations exhibited distinct marker expression and functional enrichment profiles. (A) Violin plots showing the expression of representative marker genes for CPTC-C1 (*Jun, Fos, and Atf3*) and CPTC-C4 (*Cd44, Thy1, and Postn*) across CPTC subpopulations in CG. (B) GO analysis of marker genes expressed at higher levels in each CPTC subpopulation relative to the remaining subpopulations. (C) SEM revealed that isolated CPTCs *in vitro* exhibited a well-developed microfilament cytoskeletal architecture.

Figure S4. Acupuncture enhanced predicted intercellular signaling involving CPTC-C4. (A) CellChat heatmap showing differences in predicted interaction strength between AG and CG. (B) Scatter plots showing the outgoing and incoming interaction strengths of individual cell populations in CG and AG. (C) Circle plots showing differences in the number (left) and strength (right) of predicted interactions among

CPTC subpopulations. Red and blue edges indicate increases and decreases, respectively, in AG relative to CG. (D) Bubble plot showing predicted *Fn1*–(*Itga5*+*Itgb1*) communication from each CPTC subpopulation to CPTC-C4 in AG and CG. (E) NicheNet analysis with CPTC-C0–CPTC-C3 as candidate senders and CPTC-C4 as the receiver. The left panel ranks candidate ligands by Pearson correlation-based ligand activity scores. The middle panel shows ligand expression across sender populations. The right panel shows the predicted regulatory potential of ligand–target relationships in CPTC-C4, with darker purple indicating higher regulatory potential.

Figure S5. Cyclic stretching induced ultrastructural remodeling in CPTCs. Representative TEM images showing cell morphology, Mi, caveolae, and rER in the two groups of CPTCs. Stretched CPTCs exhibited an elongated, spindle-shaped morphology, elongated Mi, increased caveolae (blue arrows), and dilation of rER cisternae. Boxed regions are shown at higher magnification. The lower panels show quantification of mitochondrial cross-sectional area and length (n = 4). **P < 0.01 and ***P < 0.001. Mi: mitochondria; rER: rough endoplasmic reticulum.

Table S1 siRNA sequences

Targets		Sequence (5’ to 3’)
Itgb1 siRNA-1	sense	CCACAGAAGUUUACAUUAATT
	antisense	UUAAUGUAAACUUCUGUGGTT
Itgb1 siRNA-2	sense	GCGAGUGUGAUAACUUCAATT
	antisense	UUGAAGUUAUCACACUCGCTT
Itgb1 siRNA-3	sense	CCGACAUCAUCCCAAUUGUTT
	antisense	ACAAUUGGGAUGAUGUCGGTT
Itgb1 siRNA-4	sense	CAGCCCAUUUAGCUACAAATT
	antisense	UUUGUAGCUAAAUGGGCUGTT

Table S2 Primers for qPCR

Primers	Sequence (5’ to 3’)
Itgb1-forward	AACTTGTTGGTCAGCAACGC
Itgb1-reverse	AACCGCAACCTGCATGATTG
Gapdh-forward	AACGACCCCTTCATTGACCTC
Gapdh-reverse	ACTGTGCCGTTGAATTTGCC

Supplementary Files

This is a list of supplementary files associated with this preprint. Click to download.

- TableS7stretchvsstaticcontrol.GO.level2Classification.xlsx
- TableS4CPTCsAGvsCGKEGGGSEA.csv
- TableS5CPTCC4AGvsCGKEGGanalysis.csv
- TableS6CPTCC4AGvsCGKEGGGSEA.csv
- originalblots.pdf
- TableS3CPTCsAGvsCGGOanalysis.csv
- TableS8stretchvsstaticcontrolKEGG.enrichment.xlsx